The Gaussian Process Hilbert Transform (GP-HT): Testing the Consistency of Electrochemical Impedance Spectroscopy Data

Francesco Ciucci[a,b,†]

[a] Department of Mechanical and Aerospace Engineering, The Hong Kong University of Science and Technology, Hong Kong, China

[b] Department of Chemical and Biological Engineering, The Hong Kong University of Science and Technology, Hong Kong, China

[†]Corresponding author: francesco.ciucci@ust.hk

Abstract

Electrochemical impedance spectroscopy (EIS) is an experimental technique that is frequently used in electrochemistry. While measuring EIS spectra is relatively simple, the interpretation of the data is hindered if the electrochemical system under study is not linear, causal, stable, and time invariant. These requirements can be assessed by applying the Kramers-Kronig relations or Hilbert transform (HT) to the EIS data. Here, we develop a new probabilistic approach to compute the HT of impedance spectra. The method, called the Gaussian process Hilbert transform (GP-HT), leverages Gaussian processes that are constrained to comply with the HT. The GP-HT, which is an infinite-dimensional generalization of previously developed Bayesian HT, is used to predict the credible intervals of the real part of the EIS spectrum from its imaginary component. The quality of the measurements can then be assessed by benchmarking the prediction against the real part of the experimental EIS spectrum. It is foreseen that, as a new approach for calculating the HT, the GP-HT will stimulate more research on the probabilistic interpretation of the EIS and its consistency.

Keywords: Electrochemical Impedance Spectroscopy, Gaussian Processes, Hilbert Transform, Kramers-Kronig relations

1 Introduction

Electrochemical impedance spectroscopy (EIS) is one of the experimental techniques most frequently used in electrochemistry.[1, 2] This technique is popular because it can lead to insight across several timescales. A typical EIS spectrum spans frequencies from a fraction of a mHz to tens of MHz. Further, EIS spectra can be measured rather quickly and reliably with modern impedance analyzers. For these reasons, EIS has been applied to fields as diverse as fuel cells,[3-5] batteries,[6-8] solar cells,[9, 10] photoelectrochemical cells,[11] sensors,[12] water-splitting,[13] corrosion,[14, 15] biosensors,[16] biology,[17, 18] cancer diagnostics,[19] and medicine.[20, 21]

The analysis of EIS spectra can lead to a wealth of information. However, the insight gained depends on the quality of the data available.[22] In general, to have a reliable spectrum, three fundamental conditions need to hold: 1) the electrochemical system under study has to be probed around a steady-state or time-invariant condition; 2) causality needs to be satisfied; and 3) the EIS measurement needs to be stable and to originate from a linear perturbation.[23, 24] To check if these requirements are met, one can repeat the measurements using different input signals or evaluate if higher harmonics are generated.[25] However, these tests are time-consuming and often not directly available in commercial impedance analyzers. Another option is to compute an integral that checks if the measured EIS spectrum complies with the Kramers-Kronig (KK) relations.[23, 24] These relations link the real and imaginary parts of the impedance as follows:[24, 26]

$$Z_{\mathrm{re}}(\omega) = Z_{\mathrm{re}}(\infty) + \frac{2}{\pi} P \int_0^\infty \frac{\widehat{\omega} Z_{\mathrm{im}}(\widehat{\omega}) - \omega Z_{\mathrm{im}}(\omega)}{\widehat{\omega}^2 - \omega^2} d\widehat{\omega} \tag{1a}$$

$$Z_{\mathrm{im}}(\omega) = -\frac{2\omega}{\pi} P \int_{-\infty}^\infty \frac{Z_{\mathrm{re}}(\widehat{\omega}) - Z_{\mathrm{re}}(\omega)}{\widehat{\omega}^2 - \omega^2} d\widehat{\omega} \tag{1b}$$

where ω is the angular frequency ($\omega = 2\pi f$ where f is the frequency) and $P = \int_{-\infty}^{\infty}(\cdot)d\hat{\omega}$ designates the Cauchy principal value. As will be explained in Section 2.1, one can note that the KK relations are nothing but the Hilbert transform (HT) of even or odd functions. [27]

Several methods have been developed to test if a particular EIS spectrum conforms to the KK relations or, equivalently, the HT, including the fitting of generalized Voigt and ladder models,[25, 28-31] and direct integration[26, 32, 33] or fast Fourier transform of the data.[34] While the EIS spectra are affected by the experimental errors and for this reason are a realization of a random variable (RV), there are only a few works that interpret the KK or HT of EIS data probabilistically.[31, 35-37] Notably, the Orazem[31, 35] and V. Pérez-Herranz[36] groups took the perspective of frequentist statistics; they utilized Monte-Carlo simulations to determine the confidence interval of the KK transform of EIS spectra.

This year our group developed the Bayesian Hilbert transform (BHT) method,[37] which interpolates (probabilistically) the EIS data using the distribution of relaxation times (DRT) model given by [38-41]

$$Z(\omega) = i\omega L_0 + R_\infty + \int_{-\infty}^{\infty} \frac{1}{1 + i\,\omega\tau}\,\gamma(\log\tau)d\log\tau \qquad (2)$$

where i is the imaginary number, L_0 and R_∞ are the inductance and resistance, respectively, and $\gamma(\log\tau)$ is the latent DRT. The idea of the BHT method is to 1) regress the real and imaginary parts of the EIS data separately using a linear and regularized DRT-based model; 2) compute the HTs of the corresponding models analytically; and 3) compare the obtained HTs with the experimental data. The BHT is probabilistic with both the fitted EIS model and its HT being multivariate RVs. While the BHT method works well for the tested cases, there is room for improvement as the BHT employs a finite basis to interpolate (2) and determine the HT. GPs overcome both limitations by providing a non-parametric paradigm for regression and

prediction.[42, 43] In fact, they can be understood as infinite-dimensional generalizations of multivariate Gaussian RVs. In addition to that, the kernel of the GP can be tailored to satisfy not only with the DRT model but also with more general HT-compliant approximations. More details on the Gaussian process Hilbert transform (GP-HT) will be given in Section 2. Lastly, we must stress that the hyperparameters of GP-HT are not chosen arbitrarily but can be optimized by maximizing the experimental evidence, loosely speaking the probability of the experimental data.[44, 45]

Leveraging GPs, this article puts forth several advancements in the analysis of EIS data through the HT. First, we formulated the HT of the EIS within the context of GPs, which are non-parametric, infinite-dimensional and provide credible intervals. Second, we developed a set of kernels that are constrained to satisfy the HT, and that can work well for logarithmically spaced frequencies. One important point to note is that the GP-HT can be further expanded following the methodology developed herein. This can be done, for example, by constructing new kernels[46] or adding depth to the GP.[47] For this reason, we foresee that this article will serve as a starting point for the development of other probabilistic and GP-inspired HT and KK-based frameworks.

2 Theory

In this section, after introducing some background concepts, we will construct GPs and associated kernels that are constrained to comply with the HT. Using the developed GP-HT framework, we will then predict the real component of the EIS spectrum from its imaginary part. The GP-HT will finally be extended to work with the admittance, *i.e.*, the inverse of the impedance.

2.1 Hilbert Transform

Let us first define the HT.[27] Take an analytic function $h(z): \mathbb{C} \to \mathbb{C}$, the HT of $h(\omega)$ for $\omega \in \mathbb{R}$ is defined as

$$Hh(\omega) = \frac{1}{\pi} P \int_{-\infty}^{\infty} \frac{h(\hat{\omega})}{\omega - \hat{\omega}} d\hat{\omega} \tag{3}$$

If $h(z)$ is an impedance transfer function[27] that is finite and approaches 0 faster than $\frac{1}{|z|}$ when $z \to \infty$, then the following two equations hold:[27, 37]

$$H\, h_{\mathrm{re}}(\omega) = -h_{\mathrm{im}}(\omega) \tag{4a}$$

$$H\, h_{\mathrm{im}}(\omega) = h_{\mathrm{re}}(\omega) \tag{4b}$$

where $h_{\mathrm{re}}(\omega) = \mathrm{Re}\big(h(\omega)\big)$ is even and $h_{\mathrm{im}}(\omega) = \mathrm{Im}\big(h(\omega)\big)$ is odd. The parity of the functions $h_{\mathrm{re}}(\omega)$ and $h_{\mathrm{im}}(\omega)$ implies that the equations (4) are equivalent to the KK relations.[27]

2.2 Distribution of Relaxation Times

We are going to use a DRT model slightly different from the one used in the BHT article[37] and assume that[38, 48]

$$Z(\omega) = i\omega L_0 + R_\infty + \int_0^{\infty} \psi(\omega, \tau)\, g(\tau) d\tau \tag{5}$$

where $\psi(\omega, \tau) = \frac{1}{1 + i\,\omega\tau}$ and $g(\tau)$ is the distribution of timescales. One notes that $\gamma(\log \tau) = \tau g(\tau)$. The reason for employing (5) rather than (2) is that, if (2) is used, then one of the DRT kernels that will be developed in Section 2.4.1 is infinite.

2.3 Gaussian Processes

We can define a GP, $h(\omega) \sim \mathcal{GP}\big(m(\omega), k(\omega, \omega')\big)$, as a generalization of multivariable RVs over functions such that, for every combination of ω and ω', $h(\omega)$ and $h(\omega')$ are bivariate Gaussians with mean and kernel defined as $m(\omega) = \mathbb{E}[h(\omega)]$ and $k(\omega, \omega') = \mathbb{E}\big[\big(h(\omega) - m(\omega)\big)\big(h(\omega') - m(\omega')\big)\big]$, respectively, and where $\mathbb{E}[\cdot]$ indicates the expectation.[39, 42, 43] Let us set $\boldsymbol{\omega} = (\omega_1, \omega_2, \ldots, \omega_N)^\top$ and define

$$h(\boldsymbol{\omega}) = (h(\omega_1), h(\omega_2), \ldots, h(\omega_N))^\top \tag{6a}$$

$$m(\boldsymbol{\omega}) = (m(\omega_1), m(\omega_2), \ldots, m(\omega_N))^\top \tag{6b}$$

$$\boldsymbol{K} = k(\boldsymbol{\omega}, \boldsymbol{\omega}) = \begin{pmatrix} k(\omega_1, \omega_1) & k(\omega_1, \omega_2) & \cdots & k(\omega_1, \omega_N) \\ k(\omega_2, \omega_1) & k(\omega_2, \omega_2) & \cdots & k(\omega_2, \omega_N) \\ \vdots & \vdots & \ddots & \vdots \\ k(\omega_N, \omega_1) & k(\omega_N, \omega_2) & \cdots & k(\omega_N, \omega_N) \end{pmatrix} \tag{6c}$$

it follows that $h(\boldsymbol{\omega})$ is a multivariate normal RV with mean $m(\boldsymbol{\omega})$ and covariance $\boldsymbol{K}$, *i.e.,*

$$h(\boldsymbol{\omega}) \sim \mathcal{N}(m(\boldsymbol{\omega}), \boldsymbol{K}) \tag{7}$$

One striking advantage of GPs is that we can predict the RV $h(\omega_\star)$ for any angular frequency $\omega_\star$. For simplicity, let us suppose that 1) $m(\omega) = 0$; and 2) we have an experimental dataset $\mathcal{D} = \{(\omega_n, y_n), \text{for } n = 1, 2, \ldots, N\}$ for which $y_n = h(\omega_n) + \varepsilon$ and $\varepsilon \sim \sigma_n \mathcal{N}(0, 1)$, where σ_n is the standard deviation of the experimental error. Then, the experimental values $\boldsymbol{y} = (y_1, y_2, \ldots, y_N)^T$ and $h(\omega_\star)$ are also part of a multivariate normal RVs with the following distribution: [42, 43]

$$\begin{pmatrix} \boldsymbol{y} \\ h(\omega_\star) \end{pmatrix} \sim \mathcal{N}\left(0, \begin{matrix} \boldsymbol{K} + \sigma_n^2 \boldsymbol{I} & \boldsymbol{k}_\star \\ \boldsymbol{k}_\star^\top & k_{\star\star} \end{matrix}\right) \tag{8}$$

7

where $\boldsymbol{I}$ is the identity matrix, $\boldsymbol{k}_\star = k(\boldsymbol{\omega}, \omega_\star) = \big(k(\omega_1, \omega_\star), k(\omega_2, \omega_\star), \dots, k(\omega_N, \omega_\star)\big)^\top$, and $k_{\star\star} = k(\omega_\star, \omega_\star)$. From (8), we can determine the probability distribution of $h(\omega_\star)$ given the dataset $\mathcal{D}$. Specifically, we will be able to obtain the predicted $h(\omega_\star)$ conditioned to the experimental data. Formally, we can write $h(\omega_\star)|\boldsymbol{y} \sim \mathcal{N}(\mu_\star, \Sigma_\star)$ with

$$\mu_\star = \boldsymbol{k}_\star^\top (\boldsymbol{K} + \sigma_n^2 \boldsymbol{I})^{-1} \boldsymbol{y} \tag{9a}$$

$$\Sigma_\star = k_{\star\star} - \boldsymbol{k}_\star^\top (\boldsymbol{K} + \sigma_n^2 \boldsymbol{I})^{-1} \boldsymbol{k}_\star \tag{9b}$$

So far, we have conventionally assumed that data and prediction are characterized by the same kernel. Let us now apply a linear transformation $\mathcal{L}_\omega(\cdot)$, like the HT in (4), to $h(\omega)$ to get a new function $j(\omega) = \mathcal{L}_\omega\big(h(\omega)\big)$. Since a linear transformation of a GP is another GP,[42, 49, 50] we can write

$$\binom{h(\omega)}{j(\omega)} \sim \mathcal{GP}\left(\binom{m(\omega)}{\mathcal{L}_\omega(m(\omega))}, \begin{matrix} k(\omega, \omega') & \mathcal{L}_{\omega'}\big(k(\omega, \omega')\big) \\ \mathcal{L}_\omega\big(k(\omega, \omega')\big) & \mathcal{L}_\omega\big(\mathcal{L}_{\omega'}\big(k(\omega, \omega')\big)\big) \end{matrix} \right) \tag{10}$$

This last equation implies that the derived kernels comply with $\mathcal{L}_\omega(\cdot)$.[39, 49, 51-54]

Let us take $h(\omega) = Z_{\mathrm{im}}(\omega)$ and $\mathcal{L}_\omega(\cdot) = H_\omega(\cdot)$, then following (4) and (10) $j(\omega) = Z_{\mathrm{re}}(\omega)$. Further, if we set $\boldsymbol{y} = Z_{\mathrm{exp,im}}(\boldsymbol{\omega}) = \big(Z_{\mathrm{exp,im}}(\omega_1), Z_{\mathrm{exp,im}}(\omega_2), \dots, Z_{\mathrm{exp,im}}(\omega_N)\big)^\top$, we can use (8) and (9) with the kernels derived by applying $\mathcal{L}_\omega(\cdot)$ as in (10) to predict $Z_{\mathrm{re}}(\omega_\star)$. After that, we can compare the predicted $Z_{\mathrm{re}}(\omega_\star)$ for $\omega_\star \in \{\omega_1, \omega_2, \dots, \omega_N\}$ against the real part of the experimental data $Z_{\mathrm{exp,re}}(\boldsymbol{\omega}) = \big(Z_{\mathrm{exp,re}}(\omega_1), Z_{\mathrm{exp,re}}(\omega_2), \dots, Z_{\mathrm{exp,re}}(\omega_N)\big)^\top$. In a nutshell, GPs can compute the HT and validate EIS data. More details will be given in Section 2.5 with the relevant companion code available on GitHub.[55]

2.4 Hilbert-transform-constrained Kernels

The main challenge of the GP-HT method is that kernels satisfying the properties of the HT, as outlined in Sections 2.1 and 2.3, are needed. To clarify this point, let us take the real and imaginary parts of the impedance, $Z_{re}(\omega)$ and $Z_{im}(\omega)$, to be part of a multivalued GP. For notational convenience, we will drop the resistive and inductive terms and write generically

$$\begin{pmatrix} Z_{re}(\omega) \\ Z_{im}(\omega) \end{pmatrix} \sim \mathcal{GP}\left(0, \begin{pmatrix} k_{re}(\omega,\omega') & k_{re-im}(\omega,\omega') \\ k_{im-re}(\omega,\omega') & k_{im}(\omega,\omega') \end{pmatrix}\right) \tag{11}$$

To ensure that the above kernels comply with the HT, we will constrain them to satisfy (4) and (10), *i.e.*,

$$k_{re-im}(\omega,\omega') = -H_{\omega'}k_{re}(\omega,\omega') \tag{12a}$$

$$k_{im-re}(\omega,\omega') = -H_{\omega}k_{re}(\omega,\omega') \tag{12b}$$

$$k_{im}(\omega,\omega') = H_{\omega}\big(H_{\omega'}k_{re}(\omega,\omega')\big) \tag{12c}$$

where the subscript ω in $H_{\omega}(\cdot)$ indicates that the HT is calculated with respect to the ω variable only. Furthermore, the kernel will need to preserve the parity of the impedance function, *i.e.*, $k_{re}(\omega,\omega') = k_{re}(\omega,-\omega')$ and $k_{im}(\omega,\omega') = -k_{im}(\omega,-\omega')$, as well as the symmetry of the covariances, *i.e.*, $k_{re}(\omega,\omega') = k_{re}(\omega',\omega)$, $k_{im}(\omega,\omega') = k_{im}(\omega',\omega)$, and $k_{re-im}(\omega,\omega') = k_{im-re}(\omega',\omega)$. To build such kernels, we will take two approaches. First, we will leverage the DRT. Second, we will start from a stationary kernel, $k_0(\omega-\omega')$, and derive a set of non-stationary kernels, *i.e.*, $k_{re}(\omega,\omega')$, $k_{re-im}(\omega,\omega')$, $k_{im-re}(\omega,\omega')$, and $k_{im}(\omega,\omega')$, from (12) as well as parity and symmetry. It is important to note that the sum of these DRT- and stationary-based kernels will also be kernels. The sum of the two kernels will be used for the analysis of some real experiments as it leads to a slight improvement of the evidence.

2.4.1 DRT-based Kernel

In this section, we will construct an HT-compliant kernel from the DRT model (5). We note that for the $\psi(\omega, \tau) = \frac{1}{1+i\,\omega\tau}$ defined above, the following holds

$$H_\omega\big(\psi(\omega, \tau)\big) = i\,\psi(\omega, \tau) \tag{13}$$

If we discard the $i\omega L_0$ and R_0 terms, then the use of (13) in (5) yields

$$HZ(\omega) = i \int_0^\infty \psi(\omega, \tau)\, g(\tau) d\tau \tag{14}$$

For the sake of a preliminary derivation, let us further assume the following finite and Voigt-like expansion of the $g(\tau)$:[24, 56]

$$g(\tau) = \sum_{n=1}^N g_n \delta(\tau - \tau_n) \tag{15}$$

where $\delta(\cdot)$ is the Dirac distribution centered at $\tau_n > 0$ and the g_n's are independent and identically distributed Gaussian RVs such that $g_n \sim \mathcal{N}\left(0, \frac{\sigma_f^2}{N}\right)$. It follows that $\mathbb{E}[g_m g_n] = \frac{\sigma_f^2}{N} \delta_{mn}$.

Substituting (15) in (5) (with, again, the terns $i\omega L_0$ and R_0 discarded) allows us to write

$$Z(\omega) = \sum_{n=1}^N g_n \psi(\omega, \tau_n) \tag{16}$$

To keep the derivation simple, we will get the kernels of the real and imaginary parts separately. For the real part,

$$Z_{\text{re}}(\omega) = \sum_{n=1}^{N} g_n \psi_{\text{re}}(\omega, \tau_n) \tag{17}$$

It follows that the expectation is $\mathbb{E}[Z_{\text{re}}(\omega)] = 0$ and the covariance is

$$
\begin{aligned}
k_{\text{DRT,re}}(\omega, \omega') &= \mathbb{E}[Z_{\text{re}}(\omega)Z_{\text{re}}(\omega')] \\
&= \sum_{m=1}^{N}\sum_{n=1}^{N} \mathbb{E}[g_m g_n]\psi_{\text{re}}(\omega, \tau_m)\,\psi_{\text{re}}(\omega', \tau_n) \\
&= \frac{\sigma_f^2}{N}\sum_{n=1}^{N} \psi_{\text{re}}(\omega, \tau_n)\,\psi_{\text{re}}(\omega', \tau_n)
\end{aligned}
\tag{18}
$$

Similarly, we can write $\mathbb{E}[Z_{\text{im}}(\omega)] = 0$ and

$$k_{\text{DRT,im}}(\omega, \omega') = \mathbb{E}[Z_{\text{im}}(\omega)Z_{\text{im}}(\omega')] = \frac{\sigma_f^2}{N}\sum_{n=1}^{N} \psi_{\text{im}}(\omega, \tau_n)\,\psi_{\text{im}}(\omega', \tau_n) \tag{19a}$$

$$k_{\text{DRT,re}-\text{im}}(\omega, \omega') = \mathbb{E}[Z_{\text{re}}(\omega)Z_{\text{im}}(\omega')] = \frac{\sigma_f^2}{N}\sum_{n=1}^{N} \psi_{\text{re}}(\omega, \tau_n)\,\psi_{\text{im}}(\omega', \tau_n) \tag{19b}$$

$$k_{\text{DRT,im}-\text{re}}(\omega, \omega') = \mathbb{E}[Z_{\text{im}}(\omega)Z_{\text{re}}(\omega')] = \frac{\sigma_f^2}{N}\sum_{n=1}^{N} \psi_{\text{im}}(\omega, \tau_n)\,\psi_{\text{re}}(\omega', \tau_n) \tag{19c}$$

Let un now relax the assumption (15) and take a continuous parametrization of the $\psi(\omega, \tau)$'s. This continuous parametrization corresponds to taking the limit $N \to \infty$ in the above equations. For example, we will be able to rewrite (18) as[1]

---

[1] Technically, $k_{\text{DRT,re}}(\omega, \omega')$ is obtained by taking $g(\tau)$ to be a GP with a white noise kernel, i.e., $\mathbb{E}[g(\tau)] = 0$ and $\mathbb{E}[g(\tau)g(\tau')] = \sigma_f^2 \delta(\tau - \tau')$.

$$k_{\text{DRT,re}}(\omega, \omega') = \sigma_f^2 \int_0^\infty \psi_{\text{re}}(\omega, \tau)\psi_{\text{re}}(\omega', \tau)\, d\tau$$

$$= \sigma_f^2 \frac{\pi}{2} \frac{1}{|\omega| + |\omega'|}$$

(20)

Therefore, we will be able to write:

$$Z_{\text{re}}(\omega) \sim \mathcal{GP}\left(0, k_{\text{DRT,re}}(\omega, \omega')\right)$$

(21)

The other pairs, see (19), follow:

$$k_{\text{DRT,im}}(\omega, \omega') = \sigma_f^2 \int_0^\infty \psi_{\text{im}}(\omega, \tau)\psi_{\text{im}}(\omega', \tau)\, d\tau$$

$$= \sigma_f^2 \frac{\pi}{2} \frac{\text{sgn}(\omega\,\omega')}{|\omega| + |\omega'|}$$

(22a)

$$k_{\text{DRT,re}-\text{im}}(\omega, \omega') = \sigma_f^2 \int_0^\infty \psi_{\text{re}}(\omega, \tau)\psi_{\text{im}}(\omega', \tau)\, d\tau$$

$$= -\sigma_f^2 \frac{\omega'}{\omega^2 - \omega'^2} \log\left|\frac{\omega}{\omega'}\right|$$

(22b)

$$k_{\text{DRT,im}-\text{re}}(\omega, \omega') = \sigma_f^2 \int_0^\infty \psi_{\text{im}}(\omega, \tau)\psi_{\text{re}}(\omega', \tau)\, d\tau$$

$$= -\sigma_f^2 \frac{\omega}{\omega^2 - \omega'^2} \log\left|\frac{\omega}{\omega'}\right|$$

(22c)

From (13), we can verify that the kernels (20), (21), and (22) comply with (11) and (12) as

$$-H_{\omega'} k_{\text{DRT,re}}(\omega, \omega') = \sigma_f^2 \int_0^\infty \psi_{\text{re}}(\omega, \tau)(-H_{\omega'}\psi_{\text{re}}(\omega', \tau)\,)d\tau$$

$$= \sigma_f^2 \int_0^\infty \psi_{\text{re}}(\omega, \tau)\psi_{\text{im}}(\omega', \tau)\, d\tau$$

(23)

$$= k_{\text{DRT,re}-\text{im}}(\omega, \omega')$$

We can also write that

$$-H_\omega k_{\text{DRT,re}}(\omega, \omega') = \sigma_f^2 \int_0^\infty \left(-H_\omega \psi_{\text{re}}(\omega, \tau)\right) \psi_{\text{re}}(\omega', \tau)\, d\tau$$

$$= \sigma_f^2 \int_0^\infty \psi_{\text{im}}(\omega, \tau) \psi_{\text{re}}(\omega', \tau)\, d\tau \tag{24}$$

$$= k_{\text{DRT,im-re}}(\omega, \omega')$$

and that

$$H_\omega \left(H_{\omega'}\, k_{\text{DRT,re}}(\omega, \omega')\right) = -\sigma_f^2 H_\omega \left(\int_0^\infty \psi_{\text{re}}(\omega, \tau)(-H_{\omega'}\psi_{\text{re}}(\omega', \tau))\, d\tau\right)$$

$$= \sigma_f^2 \int_0^\infty \left(-H_\omega \psi_{\text{re}}(\omega, \tau)\right) \psi_{\text{im}}(\omega', \tau)\, d\tau \tag{25}$$

$$= \sigma_f^2 \int_0^\infty \psi_{\text{im}}(\omega, \tau) \psi_{\text{im}}(\omega', \tau)\, d\tau$$

$$= k_{\text{DRT,im}}(\omega, \omega')$$

In addition, the developed covariance matrix preserves the parity of the real and imaginary components of the impedance, *i.e.*, $Z_{\text{re}}(\omega)$ is even and $Z_{\text{im}}(\omega)$ is odd, as:

$$k_{\text{DRT,re}}(\omega, \omega') = k_{\text{DRT,re}}(\omega, -\omega') \tag{26a}$$

$$k_{\text{DRT,im}}(\omega, \omega') = -k_{\text{DRT,im}}(\omega, -\omega') \tag{26b}$$

Therefore, the DRT-based kernel matrix complies with the basic characteristics of the impedance and corresponding HT.

2.4.2 Kernel Derived from Stationary Kernels

Let us define the kernel matrix by applying (12) directly. Since $Z_{re}(\omega)$ is an even function, $k_{re}(\omega, \omega')$ cannot be stationary. However, we can use a stationary kernel $k_0(\omega - \omega')$ with $k_0(\omega - \omega') = k_0(\omega' - \omega)$ to write an even kernel, $k_{SB,re}(\omega, \omega')$,[2] as follows:

$$k_{SB,re}(\omega, \omega') = k_0(\omega - \omega') + k_0(\omega + \omega') \tag{27}$$

Before calculating the off-diagonal terms $k_{SB,re-im}$ and $k_{SB,im-re}$, we will define

$$k_0^H(\omega) = H_\omega k_0(\omega) \tag{28}$$

and note that for any real number a

$$k_0^H(\omega + a) = H_\omega k_0(\omega + a) \tag{29}$$

Therefore

$$\begin{aligned} k_{SB,re-im}(\omega, \omega') &= -H_{\omega'} k_{SB,re}(\omega, \omega') \\ &= -H_{\omega'} k_0(\omega' - \omega) - H_{\omega'} k_0(\omega + \omega') \\ &= -k_0^H(\omega' - \omega) - k_0^H(\omega + \omega') \end{aligned} \tag{30}$$

and

$$\begin{aligned} k_{SB,im-re}(\omega, \omega') &= -H_\omega k_{SB,re}(\omega, \omega') \\ &= -H_\omega k_0(\omega - \omega') - H_\omega k_0(\omega + \omega') \\ &= -k_0^H(\omega - \omega') - k_0^H(\omega + \omega') \end{aligned} \tag{31}$$

---

[2] The subscript SB stands for stationary-based.

The other diagonal component of the kernel matrix, $k_{\text{SB,im}}(\omega, \omega')$, can be obtained by noting that $H^2 f(x) = -f(x)$ and $Hf(-x) = -Hf(y)|_{-x}$

$$
\begin{aligned}
k_{\text{SB,im}}(\omega, \omega') &= H_\omega \left(H_{\omega'} k_{\text{SB,re}}(\omega, \omega') \right) \\
&= H_\omega k_0^H(\omega' - \omega) + H_\omega k_0^H(\omega + \omega') \\
&= k_0(\omega - \omega') - k_0(\omega + \omega')
\end{aligned} \tag{32}
$$

which is odd since $k_{\text{SB,im}}(\omega, \omega') = -k_{\text{SB,im}}(\omega, -\omega')$. From (27), (30), (31), and (32) it is apparent that one only needs to calculate $k_0(\omega)$ and $k_0^H(\omega)$ to get all covariances of the GP (11). For example, in the case of the inverse quadratic stationary-based (IQ-SB) kernel, we can write[27]

$$
k_0(\omega) = \sigma_S^2 \frac{2l^2}{2l^2 + \omega^2} \tag{33a}
$$

$$
k_0^H(\omega) = \sigma_S^2 \frac{\sqrt{2}\, l\omega}{2l^2 + \omega^2} \tag{33b}
$$

where σ_S and l are two scalars. Analogous analytical expressions can be found for other kernels.[27]

2.4.3 Admittance Kernels

The framework developed in the two preceding sections assumes that the EIS spectrum is stable and therefore is finite over the entire frequency range.[23, 24] For this reason, the approach presented above cannot be directly applied to EIS data that is unbounded. However, we can reuse (with modifications) some of the concepts presented to handle unbounded EIS spectra. For instance, at the place of the impedance, we can use the admittance, which is defined as $Y(\omega) = \frac{1}{Z(\omega)}$. In order to derive a kernel similar to the one of Section 2.4.1, we will need a

model for $Y(\omega)$. Specifically, we will employ the ladder or distribution of capacitive time (DCT) model proposed by Boukamp [29] and write

$$Y(\omega) = i\omega C_0 + \frac{1}{R_\infty} + \int_0^\infty \chi(\omega, \tau) c(\tau) d\tau \tag{34}$$

where C_0 is a capacitance, $\chi(\omega, \tau) = \frac{i\omega}{1+i\omega\tau}$, and $c(\tau)$ is a latent DCT. We note that discarding the non-integral terms in (34) leads to the following (improper[3]) HT of $Y(\omega)$

$$HY(\omega) = \int_0^\infty H_\omega\big(\chi(\omega, \tau)\big) c(\tau) d\tau$$

$$= -i \int_0^\infty \chi(\omega, \tau) c(\tau) d\tau \tag{35}$$

If we take $c(\tau)$ to be a GP with a white noise kernel, *i.e.*, $\mathbb{E}[c(\tau)] = 0$ and $\mathbb{E}[c(\tau)c(\tau')] = \sigma_f^2 \delta(\tau - \tau')$, we can write

$$\begin{pmatrix} Y_{\mathrm{re}}(\omega) \\ Y_{\mathrm{im}}(\omega) \end{pmatrix} \sim \mathcal{GP}\left(0, \begin{pmatrix} k_{\mathrm{DCT,re}}(\omega, \omega') & k_{\mathrm{DCT,re-im}}(\omega, \omega') \\ k_{\mathrm{DCT,im-re}}(\omega, \omega') & k_{\mathrm{DCT,im}}(\omega, \omega') \end{pmatrix} \right) \tag{36}$$

where

$$k_{\mathrm{DCT,re}}(\omega, \omega') = \sigma_f^2 \int_0^\infty \chi_{\mathrm{re}}(\omega, \tau) \chi_{\mathrm{re}}(\omega', \tau) \, d\tau$$

$$= \sigma_f^2 \frac{\pi}{2} \frac{|\omega \, \omega'|}{|\omega| + |\omega'|} \tag{37a}$$

$$k_{\mathrm{DCT,im}}(\omega, \omega') = \sigma_f^2 \int_0^\infty \chi_{\mathrm{im}}(\omega, \tau) \chi_{\mathrm{im}}(\omega', \tau) \, d\tau \tag{37b}$$

---

[3] A constant term is missing.

$$= \sigma_f^2 \frac{\pi}{2} \frac{\omega \, \omega'}{|\omega| + |\omega'|}$$

$$k_{\text{DCT,re-im}}(\omega, \omega') = \sigma_f^2 \int_0^\infty \chi_{\text{re}}(\omega, \tau) \chi_{\text{im}}(\omega', \tau) \, d\tau$$

$$= \sigma_f^2 \frac{\omega^2 \, \omega'}{\omega^2 - \omega'^2} \log \left| \frac{\omega}{\omega'} \right|$$

$$(37c)$$

$$k_{\text{DCT,im-re}}(\omega, \omega') = \sigma_f^2 \int_0^\infty \chi_{\text{im}}(\omega, \tau) \chi_{\text{re}}(\omega', \tau) \, d\tau$$

$$= \sigma_f^2 \frac{\omega \, \omega'^2}{\omega^2 - \omega'^2} \log \left| \frac{\omega}{\omega'} \right|$$

$$(37d)$$

Incidentally, we can note that the signs of the admittance are swapped relative to those in (4). The parity and compliance with (improper) Hilbert relations follow naturally, as in Section 2.4.1. For the SB-based kernel, the signs of the off-diagonal terms defined in Section 2.4.2 need to be reversed in light of the sign swap relative to those in (4).

2.4.4 Band-limited DRT kernels

As explained in Sections 2.4.1 and 2.4.3, to obtain the DRT and DCT kernels, we had to compute integrals containing $\psi(\omega, \tau)$ and $\chi(\omega, \tau)$ in the $[0, \infty)$ interval. While using 0 and ∞ as the integration bounds of equations (20), (22), and (37) is reasonable and consistent with the models (5) and (34), nothing prohibits from relaxing this assumption. For example, we can select $g(\tau)$ to be non-zero only in the interval $\tau_{\min} \leq \tau \leq \tau_{\max}$ so that the real part of the band-limited distribution of relaxation times (BL-DRT) kernel has the following analytical expression:

$$k_{\text{BL-DRT,re}}(\omega, \omega') = \sigma_f^2 \int_{\tau_{\min}}^{\tau_{\max}} \psi_{\text{re}}(\omega, \tau) \psi_{\text{re}}(\omega', \tau) \, d\tau$$

$$(38)$$

17

$$= \sigma_f^2 \frac{q(\omega, \omega', \tau_{\max}) - q(\omega, \omega', \tau_{\min})}{\omega^2 - \omega'^2}$$

where $q(\omega, \omega', \tau) = \omega \arctan(\tau\omega) - \omega' \arctan(\tau\omega')$.

We note that if we define $q_L(\omega, \tau) = \frac{\tau\omega}{1+\omega^2\tau^2} + \arctan(\tau\omega)$, we obtain

$$\lim_{\omega' \to \omega} k_{\text{BL-DRT,re}}(\omega, \omega') = \sigma_f^2 \frac{q_L(\omega, \tau_{\max}) - q_L(\omega, \tau_{\min})}{2\omega} \tag{39}$$

This last formula is particularly interesting because around $\omega = 0$ the (39) is bounded, *i.e.*, with $\lim_{\omega' \to \omega} k_{\text{BL-DRT,re}}(\omega, \omega') = \sigma_f^2(\tau_{\max} - \tau_{\min}) + O(\omega^2)$. Instead for (20), one obtains an infinite value as $k_{\text{DRT}}(\omega, \omega) = \frac{\pi}{2} \frac{\sigma_f^2}{|\omega|}$. The asymptotic of (39) implies that the uncertainty at low frequency for the BL-DRT kernel is lower than that of the "plain" DRT kernel. Similar results can be extended to the DCT kernel to obtain the band-limited distribution of capacitive times (BL-DCT).

2.5 The Gaussian-Process Hilbert Transform (GP-HT)

Let us now look at how one can predict the real part of the experimental EIS spectrum from its imaginary part. We will reintroduce the linear term ωL_0 from (5) and, based on the results from Section 2.3, write

$$\begin{pmatrix} Z_{\text{im}}(\omega) \\ Z_{\text{H,re}}(\omega) \end{pmatrix} \sim \mathcal{GP}\left(0, \begin{pmatrix} k_{\text{im}}(\omega, \omega') + \sigma_n^2 \delta_{\omega\omega'} & k_{\text{im-re}}(\omega, \omega') \\ k_{\text{re-im}}(\omega, \omega') & k_{\text{re}}(\omega, \omega') \end{pmatrix}\right) + \begin{pmatrix} \omega L_0 \\ 0 \end{pmatrix} \tag{40}$$

where $\delta_{\omega\omega'} = 1$ if $\omega = \omega'$ and 0 otherwise. We will assume that $L_0 \sim \mathcal{N}(0, \sigma_L^2)$ and integrate L_0 out to obtain[42]

$$\begin{pmatrix} Z_{\mathrm{im}}(\omega) \\ Z_{\mathrm{H,re}}(\omega) \end{pmatrix} \sim \mathcal{GP}\left(0, \begin{pmatrix} k_{\mathrm{im}}(\omega,\omega') + \sigma_n^2 \delta_{\omega\omega'} + \omega\omega'\sigma_L^2 & k_{\mathrm{im-re}}(\omega,\omega') \\ k_{\mathrm{re-im}}(\omega,\omega') & k_{\mathrm{re}}(\omega,\omega') \end{pmatrix}\right) \tag{41}$$

Let us take $\boldsymbol{\omega} = (\omega_1, \omega_2, \dots, \omega_N)^\top$ to be the vector of experimental angular frequencies. It follows that the imaginary part of the experimental EIS spectrum, $\boldsymbol{Z}_{\mathrm{exp,im}}(\boldsymbol{\omega}) = \left(Z_{\mathrm{exp,im}}(\omega_1), Z_{\mathrm{exp,im}}(\omega_2), \dots, Z_{\mathrm{exp,im}}(\omega_N)\right)^\top$ and the predicted $Z_{\mathrm{H,re}}(\omega_\star)$ are part of the following multivariate Gaussian RV:

$$\begin{pmatrix} \boldsymbol{Z}_{\mathrm{exp,im}}(\boldsymbol{\omega}) \\ Z_{\mathrm{H,re}}(\omega_\star) \end{pmatrix} \sim \mathcal{N}\left(0, \begin{pmatrix} \boldsymbol{K}_{\mathrm{im}} + \sigma_n^2 \boldsymbol{I} + \sigma_L^2 \boldsymbol{\omega}\boldsymbol{\omega}^\top & \boldsymbol{k}_{\mathrm{im-re},\star} \\ \boldsymbol{k}_{\mathrm{im-re},\star}^\top & k_{\mathrm{re},\star\star} \end{pmatrix}\right) \tag{42}$$

where $\boldsymbol{K}_{\mathrm{im}} = k_{\mathrm{im}}(\boldsymbol{\omega},\boldsymbol{\omega})$, $\boldsymbol{k}_{\mathrm{im-re},\star} = k_{\mathrm{im-re}}(\boldsymbol{\omega},\omega_\star)$, and $k_{\mathrm{re},\star\star} = k_{\mathrm{re}}(\omega_\star,\omega_\star)$.

As shown in Section 2.4.3, we can find analogous formulas for the admittance. By assuming $C_0 \sim \mathcal{N}(0,\sigma_C^2)$ and integrating C_0 out, we can get

$$\begin{pmatrix} \boldsymbol{Y}_{\mathrm{im}}(\boldsymbol{\omega}) \\ Y_{\mathrm{H,re}}(\omega_\star) \end{pmatrix} \sim \mathcal{N}\left(0, \begin{pmatrix} \boldsymbol{K}_{\mathrm{im}} + \sigma_n^2 \boldsymbol{I} + \sigma_C^2 \boldsymbol{\omega}\boldsymbol{\omega}^\top & \boldsymbol{k}_{\mathrm{im-re},\star} \\ \boldsymbol{k}_{\mathrm{im-re},\star}^\top & k_{\mathrm{re},\star\star} \end{pmatrix}\right) \tag{43}$$

where $\boldsymbol{K}_{\mathrm{im}} = k_{\mathrm{Y,im}}(\boldsymbol{\omega},\boldsymbol{\omega})$, $\boldsymbol{k}_{\mathrm{re-im},\star} = k_{\mathrm{Y,im-re}}(\boldsymbol{\omega},\omega_\star)$, and $k_{\mathrm{im},\star\star} = k_{\mathrm{Y,im}}(\omega_\star,\omega_\star)$.

We note that equations (42) and (43) are formally identical. Therefore, we can use the following general notation

$$\begin{pmatrix} \boldsymbol{X}(\boldsymbol{\omega}) \\ X_H(\omega_\star) \end{pmatrix} \sim \mathcal{N}\left(0, \begin{pmatrix} \boldsymbol{K} + \sigma_n^2 \boldsymbol{I} + \sigma_\beta^2 \boldsymbol{b}\boldsymbol{b}^\top & \mathcal{L}\boldsymbol{k}_\star \\ \mathcal{L}\boldsymbol{k}_\star^\top & \mathcal{L}^2 k_{\star\star} \end{pmatrix}\right) \tag{44}$$

the various terms are given in Table 1. From the (44) it ensues that

$$X_H(\omega_\star)|\boldsymbol{X}(\boldsymbol{\omega}) \sim \mathcal{N}(\mu_{X_H}, \sigma_{X_H}^2) \tag{45}$$

where

$$\mu_{X_H} = \mathcal{L} k_\star^\top \left(K + \sigma_n^2 I + \sigma_\beta^2 bb^\top\right)^{-1} X(\omega) \tag{46a}$$

$$\sigma_{X_H}^2 = \mathcal{L}^2 k_{\star\star} - \mathcal{L} k_\star^\top \left(K + \sigma_n^2 I + \sigma_\beta^2 bb^\top\right)^{-1} \mathcal{L} k_\star \tag{46b}$$

We stress that the last two terms depend on the hyperparameters $\boldsymbol{\theta} = \left(\sigma_f, \sigma_S, l, \sigma_n, \sigma_\beta\right)^\top$ used. Their optimal value can be obtained by maximizing the marginal log-likelihood or evidence defined as [42, 44, 45]

$$\log p(X(\omega)|\omega, \boldsymbol{\theta})$$

$$= -\frac{1}{2} X^\top \left(K + \sigma_n^2 I + \sigma_\beta^2 bb^\top\right)^{-1} X - \frac{1}{2}\log\left|K + \sigma_n^2 I + \sigma_\beta^2 bb^\top\right| \tag{47}$$

$$-\frac{M}{2}\log(2\pi)$$

or equivalently by minimizing negative marginal log-likelihood, i.e., $\mathcal{L}(\boldsymbol{\theta}, \omega, X) = -\log p(X(\omega)|\omega, \boldsymbol{\theta})$, to obtain the optimal $\boldsymbol{\theta}_{\text{opt}}$:

$$\boldsymbol{\theta}_{\text{opt}} = \underset{\boldsymbol{\theta}}{\text{argmin}}\, \mathcal{L}(\boldsymbol{\theta}, \omega, X(\omega)) \tag{48}$$

The GP-HT method works according to the schematic in Figure 1. We will illustrate this using the impedance as an example. First, given the imaginary part of the EIS spectrum one optimizes the hyperparameters $\boldsymbol{\theta}$ using (48). Then, with the optimal $\boldsymbol{\theta}_{\text{opt}}$ one can not only regress the imaginary part of the EIS spectrum but also predict its real part[4] using the imaginary component, see (44) and corresponding entries in Table 1. After that, the residuals and their probability

---

[4] An offset value needs to be computed. For the impedance, the following $R_\infty = \frac{1}{N}\sum_{n=1}^{N}\left(Z_{\text{exp,re}}(\omega_n) - Z_{\text{H,re}}(\omega_n)\right)$ term is added.

distribution functions (pdfs) are computed. For the admittance, the procedure is formally identical. The actual implementation is provided in a dedicated repository on GitHub.[55]

3 Results

The theory developed in Section 2 was benchmarked against various synthetic and real experiments. The use of artificial experiments is motivated by the need to check the GP-HT for consistency in well-controlled conditions. Actual experimental EIS spectra were utilized to test if the proposed method can fare well when used to analyze real experimental data.

3.1 Artificial experiments

The synthetic experiments were obtained from a stochastic process of the form

$$Z_{\text{exp}}(\omega) = Z_{\text{exact}}(\omega) + \sigma_{\text{exp}}(\varepsilon_{\text{re}} + i\ \varepsilon_{\text{im}}) \tag{49}$$

where $Z_{\text{exp}}(\omega)$ is the synthetic impedance, $Z_{\text{exact}}(\omega)$ is a known impedance spectrum, and ε_{re} and ε_{im} are independent RVs such that $\varepsilon_{\text{re}}, \varepsilon_{\text{im}} \sim \mathcal{N}(0,1)$. Unless otherwise stated, $\sigma_{\text{exp}} = 0.8\ \Omega$, the frequency range is between 10^{-4} and 10^4 Hz with a spacing of 10 points per decade. By changing $Z_{\text{exact}}(\omega)$, we will show how the GP-HT method can be used to obtain the real component of the EIS spectrum from its imaginary part. We will also outline cases where $Z_{\text{exact}}(\omega)$ is not a real transfer function and demonstrate that the GP-HT method can detect non-compliance with the HT. The artificial EIS examples used only the DRT-based kernel, $k_{\text{DRT}}(\omega, \omega')$, as no noticeable improvement was found if the $k_{\text{SB}}(\omega, \omega')$ was also utilized.

The first stochastic experiment shown is based on the ZARC,[24] a circuit element that complies with the HT relations and has the following analytical expression:

$$Z_{\text{ZARC}}(\omega) = R_\infty + \frac{R_{\text{ct}}}{1 + (i2\pi f \tau_0)^\phi} \tag{50}$$

where R_∞ and R_{ct} are the Ohmic and charge-transfer resistances, respectively, τ_0 is a timescale, and ϕ is a scalar dispersion factor. The numerical values of the parameters were chosen to be $R_\infty = 10\ \Omega$, $R_{\text{ct}} = 50\ \Omega$, $\tau_0 = 1$ s, and $\phi = 0.8$, consistently with our previous study.[37] Figure 2 (a) reports the realization of (49) with $Z_{\text{exact}}(\omega) = Z_{\text{ZARC}}(\omega)$. First, we minimized the negative log-likelihood $\mathcal{L}(\boldsymbol{\theta}, \boldsymbol{\omega}, \boldsymbol{Z}_{\text{im}})$ by solving (48) with respect to the hyperparameter vector $\boldsymbol{\theta} = \left(\sigma_n, \sigma_f\right)^\top$. For illustration, $\mathcal{L}(\boldsymbol{\theta}, \boldsymbol{\omega}, \boldsymbol{Z}_{\text{im}})$ is shown as a filled contour plot in Figure S1. There, the minimum, which was subsequently used for both regression and prediction, is indicated with a star symbol. Then, equipped with the optimal $\boldsymbol{\theta}$, we fitted the imaginary part of the synthetic EIS spectrum using the GP, see Figure 2 (b). One can note that the GP-HT closely matches $Z_{\text{exp,im}}(\omega)$. The predicted $R_\infty + Z_{\text{H,re}}(\omega)$ is presented in Figure 2 (c), where the constant R_∞ was obtained by minimizing the distance between $R_\infty + \mathbb{E}\left[Z_{\text{H,re}}(\omega)\right]$ and $Z_{\text{exp,re}}(\omega)$. The mean (solid black line) and 1σ, 2σ, and 3σ (shaded grey areas) of $R_\infty + Z_{\text{H,re}}(\omega)$ are shown. In Figure 2 (d), the dots indicate the residuals from the mean, defined as $R_\infty + \mathbb{E}\left[Z_{\text{H,re}}(\omega)\right] - Z_{\text{exp,re}}(\omega)$, and the bands show the covariance of $Z_{\text{H,re}}(\omega) - \mathbb{E}\left[Z_{\text{H,re}}(\omega)\right]$. One notices that the distribution of the residuals is symmetric with its center around zero, and the width is relatively small compared to the 1σ, 2σ, and 3σ credible bands. Consistently in Figure 2 (c)-(d), one notices a blow-up in the uncertainty towards low frequencies. Such an increase can be explained by inspecting the DRT kernel, whose real and imaginary components $k_{\text{DRT,re}}(\omega, \omega')$ and $k_{\text{DRT,im}}(\omega, \omega')$ tend to infinity when $\omega, \omega' \to 0$, see Section 2.4.1. Using $k_{\text{SB}}(\omega, \omega')$ would alleviate such an asymptotic behavior. These issues may be overcome by selecting the BL-DRT kernel described in Section 2.4.4. We took the same synthetic experiment presented in Figure 2 and changed the kernel to BL-DRT with

$\tau_{\min} = 0$ and $\tau_{\max} = 10^4, 10^3$, and 10^2 s. In Figure 3, $R_\infty + Z_{H,re}(\omega)$ and residuals are shown in panels (a) & (b), (c) & (d), and (e) & (f) for $\tau_{\max} = 10^4, 10^3$, and 10^2 s, respectively. The left-hand panels of Figure 3 compare the $R_\infty + Z_{H,re}(\omega)$ with the real part of the synthetic experiment. Residuals and distributions are shown in the right-hand-side panels. The synthetic experiment residual distribution around the mean value $R_\infty + \mathbb{E}[Z_{H,re}(\omega)]$ are sensitive to $\tau_{\max}$, but the credible bands narrow as $\tau_{\max}$ decreases.

One may also wonder if the GP-HT method can be effective in cases where the underlying EIS and DRT are characterized by frequency overlap. To test these circumstances, we chose the following sum of two ZARCs, *i.e.*,

$$Z_{2 \times ZARC}(\omega) = 2R_\infty + R_{ct} \left(\frac{1}{1 + (i2\pi f \tau_0^I)^\phi} + \frac{1}{1 + (i2\pi f \tau_0^{II})^\phi} \right) \tag{51}$$

where the parameters are identical to those used for (50) except for the two timescales $\tau_0^I = 10^{-1}$ s and $\tau_0^{II} = 10$ s. As evident in Figure S2, the GP-HT method works well as it captures the compliance with the HT correctly. A similar conclusion can be drawn from Figure S3 where the two underlying ZARCs, see Figure S3 (a) for the Nyquist plot, have an even greater frequency overlap ($\tau_0^I = 10^{-1}$ s and $\tau_0^{II} = 1$ s).

We also studied another HT-compliant circuit originating from a piecewise-constant (PWC) timescale model such that

$$Z_{PWC}(\omega) = R_\infty + \frac{R_{ct}}{\log \frac{\tau_2}{\tau_1}} \left(\log \left(1 - \frac{i}{2\pi f \tau_1} \right) - \log \left(1 - \frac{i}{2\pi f \tau_2} \right) \right) \tag{52}$$

where the two timescales τ_1 and τ_2 are chosen to be 10 s and 10^{-1} s, respectively. For this model, the DRT recovery is difficult. [57-59] Therefore, one can easily challenge the assumptions that led to the development of the DRT kernel of Section 2.4.1. A realization of (49) with

23

$Z_{\text{exact}}(\omega) = Z_{\text{PWC}}(\omega)$ is shown in the Nyquist form in Figure 4 (a). The GP-HT regression of the imaginary part of the impedance is reported in Figure 4 (b). The GP-HT and residuals are presented in Figure 4 (c) and (d), respectively. The results indicate a good recovery of the real part of the impedance and closely match those of the BHT.

Another "pathological" test case (the underlying DRT is unbounded as $\tau \uparrow \tau_0$) is the fractal element:

$$Z_{\text{fractal}}(\omega) = R_\infty + \frac{R_{\text{ct}}}{(1 + i \, 2\pi f \tau_0)^{\phi_F}} \tag{53}$$

where the dispersion $\phi_F = 0.6$. The corresponding Nyquist plot is shown in Figure S4 (a). The GP-HT regresses well the imaginary part of the impedance, see Figure S4 (b), and predicts from the imaginary part of the EIS spectrum its real component as shown in Figure S4 (c) and (d).

We then tested whether the GP-HT method can be used to detect if an EIS spectrum does not comply with the HT. To do that, we employed three examples. The first one uses (51) and applies a low-frequency drift, $\zeta(\omega, \rho)$, to one of the ZARCs, namely

$$Z_{\text{ZARC-DRIFT}}(\omega, \rho) = 2R_\infty + R_{\text{ct}} \left(\frac{1}{1 + (i2\pi f \tau_0^{\text{I}})^\phi} + \frac{1}{1 + (i2\pi f \tau_0^{\text{II}})^\phi} \zeta(\omega, \rho) \right) \tag{54}$$

where $\zeta(\omega, \rho) = \frac{1}{\log\frac{\omega_{\max}}{\omega_{\min}}} \log\left(\frac{\omega_{\max}^\rho \omega^{1-\rho}}{\omega_{\min}} \right)$, $\omega_{\min} = 2\pi \, 10^{-4}$ Hz, $\omega_{\max} = 2\pi \, 10^4$ Hz, and $\rho \geq$ 1 is a scalar. If $\rho \neq 1$, then the $Z_{\text{ZARC-DRIFT}}(\omega)$ is not a transfer function. The noiseless $Z_{\text{ZARC-DRIFT}}(\omega, \rho = 1)$ and noisy $Z_{\text{ZARC-DRIFT}}(\omega, \rho = 1.5)$ are shown in Figure 5 (a). While the regression of the imaginary part shown in Figure 5 (b) is excellent, applying the GP-HT to obtain the $R_\infty + Z_{\text{H,re}}(\omega)$ leads to severe inconsistencies as it can be seen in Figure 5 (c). These discrepancies occur at both low and high frequencies, and significantly broaden the residual

distribution, see Figure 5 (d). The other non-HT compliant EIS spectrum studied is based on the $Z_{\text{ZARC}}(\omega, \phi)$ model defined in (50) and uses $Z_{\text{ZARC-corrupt}}(\omega) = \text{Re}\big(Z_{\text{ZARC}}(\omega, 0.8)\big) + i\,\text{Im}\big(Z_{\text{ZARC}}(\omega, 0.9)\big)$ as the "exact" impedance, see Figure S5 (a) for its Nyquist plot. Even though, as shown in Figure S5 (b), the GP matches well the imaginary part of $Z_{\text{ZARC-corrupt}}(\omega)$ $R_\infty + Z_{\text{H,re}}(\omega)$ does not fit its real part, see Figure S5 (c). Deviations in the frequency range from 10 mHz to 1 Hz are particularly significant in the residual plots presented in Figure S5 (d). These examples suggest that the GP-HT can be used to identify inconsistencies in the EIS spectrum. As a final third example, we tested the GP-HT framework against a time-drifting model with the following response [60]

$$Z(\omega) = R_\infty + \frac{R_{\text{ct}}(t)}{1 + i\,\omega\,R_{\text{ct}}(t)C_0} \tag{55}$$

where $R_\infty = 50\ \Omega$, $C_0 = 2 \times 10^{-2}$ F, $R_{\text{ct}}(t) = R_0 \mp k\left(t/s\right)^{\alpha_\mp}$, $R_0 = 500\ \Omega$, $\alpha_- = 0.5$, $\alpha_+ = 2$, and $k_- = 1.5\ \Omega$ and $k_+ = 5 \times 10^{-6}\ \Omega$. Finally, the experimental EIS acquisition time, t, is defined as $t = \sum_{n=1}^{N} \frac{1}{f_n}$ where N is the total number of experimental frequencies probed with $f_1 > f_2 > \cdots > f_N$. The artificial experiments were drawn with $\sigma_{\text{exp}} = 2\ \Omega$. The Nyquist plots for the are decreasing (-) and increasing (-) R_{ct}'s are shown in Figure S6 (a) and Figure S7 (a), respectively. The regressed GP models in the respective (b) panels fit well the data. However, the GP-HT'd plots and residuals in the (c) and (d) panels of Figure S6 and Figure S7 correctly show that these artificial spectra do have a low frequency drift. This example further supports the claim that the GP-HT method can detect if an EIS spectrum does not comply with the HT.

Many experimental EIS spectra, for example, in the field of solid oxide fuel cell (SOFC), have inductive features. Therefore, it is critical to gauge if the GP-HT model can handle those. For that, we used a circuit with the following analytical impedance $Z_{\text{ZARC+L}}(\omega) = i\omega L_0 + Z_{\text{ZARC}}(\omega)$ where $L_0 = 500\ \mu F$. Figure 6 (a) shows a representative EIS spectrum. As one can

observe in Figure 6 (c) and (d), the GP-HT can accurately predict the real part of the EIS spectrum from the imaginary spectrum shown in Figure 6 (b). For $\sigma_{\text{exp}} = 0.1, 0.2, \ldots, 1$, we drew 100 artificial experiments times and conducted, for each experiment, the associated GP-HT analysis. The optimization lead to finding, among others, the hyperparameters σ_n, see Figure 6 (e), and σ_L. The hyperparameter σ_n matches well the "experimental" noise level σ_{exp}, as can be observed by the linear relation of slope=1 between the two. Also, from σ_L, we can estimate L_0 using the following expression[39, 42]

$$\bar{L}_0 = \frac{\boldsymbol{\omega}^\top (\boldsymbol{K}_{\text{im}} + \sigma_n^2 \boldsymbol{I})^{-1} \boldsymbol{Z}_{\text{exp,im}}(\boldsymbol{\omega})}{\sigma_L^{-2} + \boldsymbol{\omega}^\top (\boldsymbol{K}_{\text{im}} + \sigma_n^2 \boldsymbol{I})^{-1} \boldsymbol{\omega}} \tag{56}$$

One can observe from Figure 6 (f) that the median $\bar{L}_0$'s match well the preset value irrespective of σ_{exp}. It is worth noting that, as expected, if the noise level increases, all point estimates are characterized by greater uncertainty.

Benchmarking the GP-HT results against unbounded impedances such as the one shown in Figure 7 (a) is of critical importance as the unboundedness is a characteristic trait of the EIS response of many electrochemical devices, including batteries and supercapacitors. For this example, we used the theory established in Section 2.4.3. The exact impedance, shown in Figure 7 (a), was obtained from the nonlinear distribution of diffusion times (DDT) model[61] with identical parameters as those of another publication.[37] The impedance was transformed into an admittance and noise was added ($\sigma_{\text{exp}} = 4$ mS). The admittance spectrum is shown in Figure 7 (b). We fitted the imaginary part of $Y(\omega)$ using the BL-DCT kernel ($\tau_{\text{min}} = 10^{-6}$ s and $\tau_{\text{max}} = \infty$). One can observe in Figure 7 (c) and (d) that the GP-HT can not only closely fit the experimental $Y_{\text{im}}(\omega)$, but it can also predict $Y_{\text{re}}(\omega)$. The obtained residuals are centered around the origin and characterized by a symmetrical distribution, see Figure 7 (e), indicating, as expected and consistently with the BHT results, that this data is HT-compliant.[37]

3.2 Real Experiments

The analysis of the GP-HT model would be incomplete if we did not study real experimental data. We considered the impedance of a symmetrical SOFC with $Ba_{0.95}La_{0.05}Fe_{0.95}P_{0.05}O_{3-\delta}$ (BLFP) as the electrode.[62] The actual EIS spectrum is shown as a Nyquist plot in Figure 8 (a). After regressing the imaginary part of the impedance with the BL-DRT kernel ($\tau_{max} = 1$ s), Figure 8 (b), we computed the GP-HT to recover the real part of the EIS spectrum, see Figure 8 (c). The residual plot reported in Figure 8 (d) confirms the close similarity between the $Z_{re}(\omega)$ and $R_\infty + Z_{H,re}(\omega)$. These results agree with those previously obtained with the BHT model,[37] confirming the quality of this specific experimental spectrum. We also analyzed the impedance of a symmetric Li|composite polymer electrolyte|Li cell.[63] These data were collected from 1Hz to 900 kHz with 6 points per decade and are shown in Figure S7 (a). Figure S7 (b) reports the $Z_{im}(\omega)$ that was used to obtain the $R_\infty + Z_{H,re}(\omega)$ of Figure S7 (c). In the latter Figure one can notice a good agreement between the prediction and the real part of the experimental data. Small residuals centered around the origin were obtained, see Figure S7 (d). One should note that, for the symmetric battery example, we used a kernel that is the sum of a BL-DRT kernel with $\tau_{max} = 0.1$ s and an IQ-SB kernel.

We analyzed unbounded EIS data from batteries. In the first test, we considered the spectrum of a Na-ion battery half-cell with a $2H$-MoS_2 electrode, see the impedance and admittance in Figure 9 (a) and (b), respectively.[64] The data was taken from 0.01 Hz to 500 kHz with a spacing of 6 points per decade. The kernel was the BL-DRT kernel with $\tau_{min} = 10^{-6}$ s. The GP-HT regression matches well the imaginary part of the admittance for all frequencies probed, see Figure 9 (c). Furthermore, the GP-HT gives a $Y_{H,re}(\omega)$ that closely captures the experimental $Y_{exp,re}(\omega)$, see Figure 9 (d), with residuals that are small, symmetrically distributed, and centered around the origin, see Figure 9 (e). As a second example, we analyzed the EIS

spectrum of an Si nanowire Li-ion half-cell from an article of Ruffo and co-workers.[65] The Nyquist representation and admittance are reported in Figure S9 (a) and (b), respectively. For the GP-HT analysis, the kernel was the sum of the BL-DRT kernel with $\tau_{max} = 5 \times 10^{-5}$ s and an IQ-SB kernel. The optimized GP-HT regression, see Figure S9 (c), and GP-HT prediction, see Figure S9 (d), fit the experimental data well. The residuals shown in Figure S9 (e), are small, symmetrically distributed, and centered around the origin. These results agree with those obtained from the Bayesian-HT,[37] suggesting that the two methods are consistent.

3.3 Discussion and Future Works

The results above show that the GP-HT model is effective in evaluating the quality of EIS spectra. By generalizing normally distributed RVs over functions, the GP-HT extends the previously developed BHT method.[37] The core idea of this article is to develop kernels that, by construction, are constrained to conform to the HT. It follows that if applied to the imaginary/real part of the impedance or admittance, the GP-HT model allows us to predict the real/imaginary component. We should stress that one of the key traits of the approach is that the hyperparameters are not chosen arbitrarily but by maximizing the experimental evidence.

We should point out, however, that for the impedance tests, we were not able to use the real part of the EIS spectrum without having large deviation and uncertainties (at extremal frequencies) in the predicted imaginary component. To overcome the large uncertainty, one could replace the $\psi(\omega, \tau)$ used in Section 2.4.1 with the following

$$\tilde{\psi}(\omega, \tau) = \int_0^\infty \psi(\omega, \tau') \, \phi(\tau', \tau) \, d\tau \tag{57}$$

where $\phi(\tau', \tau)$ is, for example, a radial basis function.[40] Another option would be to use the BL-DRT kernel developed in Section 2.4.4. We did not study the BL-DRT kernel extensively, but, in principle, the hyperparameters τ_{min} and τ_{max} could be also optimized to improve the

GP-HT results. Regarding the admittance described in Section 2.4.3, an interesting option would be to use the DDT directly to compute the kernels.[66]

In the theory section, we have made the major assumption that the experimental errors consist of white noise. It would also be interesting to probe the impact of more complicated error models. One could find out how such models affect the GP-HT prediction or, conversely, if the GP-HT can be used to obtain experimental errors.[31, 67] To that end, the analysis of both artificial and real experiments is needed.

4 Conclusions

In this article, we have developed a new method for computing the HT of impedance spectra. The approach is based on constrained GPs, which not only generalize RVs to the continuum limit but also comply, by construction, with the HT. The constraints were obtained by developing various kernels based on the DRT, DCT, and stationary kernels that intrinsically satisfy the properties of impedance functions, including their parity and HT (or KK relations). The hyperparameter characteristic of the kernels can be obtained, as in the previously developed BHT, by optimization of the evidence. That is, the optimal parameters are the ones that, loosely speaking, maximize the probability of the experiment. One notable advantage of the GP-HT is that the kernels developed herein are analytical. Therefore, the calculation of matrices and derivatives is quick compared to brute force integration. The GP-HT approach was benchmarked against well-controlled synthetic experiments and real experiments. It was tested for data originating from fuel cells and batteries with both bounded and unbounded EIS spectra. The GP-HT was able to establish if the experimental impedance complies with the HT or not. HT-compliant EIS data showed good matching between the real part of the spectrum and the GP-HT prediction. Instead, corrupted data were characterized by large non-randomly-distributed residuals. In short, this work develops a completely new approach for the

29

computation of the HT and KK relations in EIS and opens up a new avenue of research for benchmarking EIS data.

Acknowledgments

List of abbreviations and symbols

BHT	Bayesian Hilbert transform
BL-DCT	Band-limited distribution of capacitive times
BL-DRT	Band-limited distribution of relaxation times
DCT	Distribution of capacitive times
DDT	Distribution of diffusion times
DRT	Distribution of relaxation times
EIS	Electrochemical impedance spectroscopy
GP	Gaussian process
GP-HT	Gaussian process Hilbert transform
HT	Hilbert transform
IQ	Inverse quadratic
IQ-SB	Inverse-quadratic stationary-based
RV	Random variable
SB	Stationary-based
f	Frequency
$g(\tau)$	Latent distribution of timescales
$\mathcal{GP}\big(m(\omega), k(\omega, \omega')\big)$	Gaussian process with mean $m(\omega)$ and kernel $k(\omega, \omega')$
H	Hilbert transform
H_ω	Hilbert transform with respect to the variable ω
i	Imaginary number
$\mathbf{I}$	Identity matrix
im	Subscript indicating the imaginary part
$k(\omega, \omega')$	Kernel
$\boldsymbol{k}_\star$	Vector from the kernel defined as $k(\boldsymbol{\omega}, \omega_\star)$
$k_{\star\star}$	Scalar defined as $k(\omega_\star, \omega_\star)$
$\boldsymbol{K}$	Matrix defined as $k(\boldsymbol{\omega}, \boldsymbol{\omega})$
l	Length scale

L_0	Inductance
$\mathcal{L}(\boldsymbol{\theta}, \boldsymbol{\omega}, \boldsymbol{Z}_{\text{exp}})$	Negative log-likelihood
N	Number of experimental points
$\mathcal{N}(\mu, \sigma^2)$	Normal random variable of mean μ and standard deviation σ
$p(\cdot)$	Probability distribution function
R_∞	Ohmic resistance
R_{ct}	Charge-transfer resistance
re	Subscript indicating the real part
$\boldsymbol{y}$	Vector containing experimental data
$\boldsymbol{Y}_{\text{exp}}$	Vector of experimental admittances
Z_{H}	HT'd admittance
$\boldsymbol{Z}_{\text{exp}}$	Vector of experimental impedances
Z_{H}	HT'd impedance
$\delta(\omega - \omega')$	Dirac distribution centered at ω'
δ_{nm}	Kronecker delta
ε	Experimental error $\sim \mathcal{N}(0, \sigma_{\text{exp}}^2)$
$\zeta(\omega, \rho)$	Drift function
$\boldsymbol{\theta}$	Vector of hyper-parameters
μ	Mean value (scalar)
$\boldsymbol{\mu}$	Mean value (vector)
ρ	Parameter for the drift function
σ_f	Parameter of the DRT or DCT kernel
σ_{exp}	Standard deviation of the experimental error (assigned)
σ_n	Standard deviation of the experimental error (hyperparameter)
σ_{SB}	Parameter of the SB kernel
Σ	Covariance (scalar)
$\boldsymbol{\Sigma}$	Covariance (matrix)
$\chi(\omega, \tau)$	Complex transfer function $= \dfrac{i\omega}{1 + i\omega\tau}$

$\psi(\omega, \tau)$	Complex transfer function $= \dfrac{1}{1+i\,\omega\tau}$
ω	Angular frequency $(\omega = 2\pi f)$
$\omega_\star$	Angular frequency of the prediction
$\boldsymbol{\omega}$	Vector of angular frequencies

References:

1. D. D. Macdonald, *Electrochim. Acta,* **51** (8-9), 1376-1388 (2006).

2. E. Barsoukov and J. R. Macdonald, *Impedance spectroscopy: theory, experiment, and applications*, Wiley-Interscience (2005).

3. A. Mroziński, S. Molin, and P. Jasiński, *Electrochim. Acta,* **346** 136285 (2020).

4. H. Schichlein, A. C. Müller, M. Voigts, A. Krügel, and E. Ivers-Tiffée, *J. Appl. Electrochem.,* **32** (8), 875-882 (2002).

5. A. Weiß, S. Schindler, S. Galbiati, M. A. Danzer, and R. Zeis, *Electrochim. Acta,* **230** 391-398 (2017).

6. D. Andre, M. Meiler, K. Steiner, C. Wimmer, T. Soczka-Guth, and D. U. Sauer, *J. Power Sources,* **196** (12), 5334-5341 (2011).

7. B. Manikandan, V. Ramar, C. Yap, and P. Balaya, *J. Power Sources,* **361** 300-309 (2017).

8. J. P. Schmidt, T. Chrobak, M. Ender, J. Illig, D. Klotz, and E. Ivers-Tiffée, *J. Power Sources,* **196** (12), 5342-5348 (2011).

9. A. Pockett, G. E. Eperon, T. Peltola, H. J. Snaith, A. Walker, L. M. Peter, and P. J. Cameron, *J. Phys. Chem. C,* **119** (7), 3456-3465 (2015).

10. F. Fabregat-Santiago, J. Bisquert, G. Garcia-Belmonte, G. Boschloo, and A. Hagfeldt, *Sol. Energy Mater. Sol. Cells,* **87** (1), 117-131 (2005).

11. T. Lopes, L. Andrade, H. A. Ribeiro, and A. Mendes, *Int. J. Hydrogen Energy,* **35** (20), 11601-11608 (2010).

12. B. Pejcic and R. De Marco, *Electrochim. Acta,* **51** (28), 6217-6229 (2006).

13. T. Lopes, L. Andrade, F. Le Formal, M. Gratzel, K. Sivula, and A. Mendes, *Phys. Chem. Chem. Phys.,* **16** (31), 16515-16523 (2014).

14. M. P. Gomes, I. Costa, N. Pébère, J. L. Rossi, B. Tribollet, and V. Vivier, *Electrochim. Acta,* **306** 61-70 (2019).

15. D. V. Ribeiro and J. C. C. Abrantes, *Constr. Build. Mater.,* **111** 98-104 (2016).

16. T. Bertok, L. Lorencova, E. Chocholova, E. Jane, A. Vikartovska, P. Kasak, and J. Tkac, *ChemElectroChem,* **6** (4), 989-1003 (2019).

17. X. Ma, X. Du, H. Li, X. Cheng, and J. C. M. Hwang, *IEEE T. Microw. Theory,* **66** (8), 3690-3696 (2018).

18. Y. Xu, X. Xie, Y. Duan, L. Wang, Z. Cheng, and J. Cheng, *Biosens. Bioelectron.,* **77** 824-836 (2016).

19. J. Malvehy, A. Hauschild, C. Curiel-Lewandrowski, P. Mohr, R. Hofmann-Wellenhof, R. Motley, C. Berking, D. Grossman, J. Paoli, C. Loquai, J. Olah, U. Reinhold, H. Wenger, T. Dirschka, S. Davis, C. Henderson, H. Rabinovitz, J. Welzel, D. Schadendorf, and U. Birgersson, *British Journal of Dermatology,* **171** (5), 1099-1107 (2014).

20. E. Kozhevnikov, X. Hou, S. Qiao, Y. Zhao, C. Li, and W. Tian, *J. Mater. Chem. B.,* **4** (16), 2757-2767 (2016).

21. J. Wu, P. Wang, Y. Tang, H. Liu, H. Wang, W. Zhang, Y. Zhang, L. Chen, Z. Xu, and X. Yao, *Med. Phys.,* **46** (5), 2522-2525 (2019).

22. F. Ciucci, *Curr. Opin. Electrochem.,* **13** 132-139 (2019).

23. M. E. Orazem and B. Tribollet, *Electrochemical impedance spectroscopy*, Wiley Interscience (2017).

24. A. Lasia, *Electrochemical impedance spectroscopy and its applications*, Springer (2014).

25. M. Schönleber, D. Klotz, and E. Ivers-Tiffée, *Electrochim. Acta,* **131** 20-27 (2014).

26. M. S. R. Urquidi‑Macdonald and D. D. Macdonald, *J. Electrochem. Soc.,* **133** (10), 2018 (1986).

27. F. W. King, *Hilbert transforms*, Cambridge University Press, Cambridge (2009).

28. B. A. Boukamp and J. Ross Macdonald, *Solid State Ionics,* **74** (1), 85-101 (1994).

29. B. A. Boukamp, *J. Electrochem. Soc.,* **142** (6), 1885 (1995).

30. P. Agarwal, M. E. Orazem, and L. H. Garcia‑Rubio, *J. Electrochem. Soc.,* **139** (7), 1917 (1992).

31. P. Agarwal, M. E. Orazem, and L. H. Garcia‑Rubio, *J. Electrochem. Soc.,* **142** (12), 4159 (1995).

32. B. A. Boukamp, *Solid State Ionics,* **62** (1), 131-141 (1993).

33. M. R. S. Urquidi-Macdonald and D. D. Macdonald, *Electrochim. Acta,* **35** (10), 1559-1566 (1990).

34. P. Bruzzoni, R. M. Carranza, J. R. Collet Lacoste, and E. A. Crespo, *Electrochim. Acta,* **48** (4), 341-347 (2002).

35. B. Hirschorn and M. E. Orazem, *J. Electrochem. Soc.,* **156** (10), C345 (2009).

36. J. J. Giner-Sanz, E. M. Ortega, and V. Pérez-Herranz, *Electrochim. Acta,* **209** 254-268 (2016).

37. J. Liu, T. H. Wan, and F. Ciucci, *10.26434/chemrxiv.12152529.v1,* (2020).

38. E. Ivers-Tiffée and A. Weber, *J. Ceram. Soc. Jpn.,* **125** (4), 193-201 (2017).

39. J. Liu and F. Ciucci, *Electrochim. Acta,* **331** 135316 (2020).

40. T. H. Wan, M. Saccoccio, C. Chen, and F. Ciucci, *Electrochim. Acta,* **184** 483-499 (2015).

41. S. Effendy, J. Song, and M. Z. Bazant, *J. Electrochem. Soc.,* **167** (10), 106508 (2020).

42. C. E. Rasmussen and C. K. I. Williams, *Gaussian processes for machine learning*, The MIT Press ((2005)).

43. K. P. Murphy, *Machine learning - a probabilistic perspective*, The MIT Press ((2012)).

44. C. M. Bishop, *Pattern recognition and machine learning*, Springer-Verlag ((2006)).

45. D. J. C. MacKay, in *Maximum Entropy and Bayesian Methods: Santa Barbara, California, U.S.A., 1993*, G. R. Heidbreder, ed., p. 43-59, Springer Netherlands, Dordrecht, (1996).

46. L. Ambrogioni and E. Maris, *Signal Process.,* **160** 215-228 (2019).

47. D. Andreas and L. Neil, p. 207-215. PMLR, 2013.

48. M. Saccoccio, T. H. Wan, C. Chen, and F. Ciucci, *Electrochim. Acta,* **147** 470-482 (2014).

49. C. Jidling, J. Hendriks, N. Wahlström, A. Gregg, T. B. Schön, C. Wensrich, and A. Wills, *Nuclear Instruments and Methods in Physics Research Section B: Beam Interactions with Materials and Atoms,* **436** 141-155 (2018).

50. S. Särkkä, *in* "Artificial Neural Networks and Machine Learning – ICANN 2011" (T. Honkela, W. Duch, M. Girolami and S. Kaski, eds.), p. 151-158. Springer Berlin Heidelberg, Berlin, Heidelberg, 2011.

51. Z. Purisha, C. Jidling, N. Wahlström, T. B. Schön, and S. Särkkä, *Inverse Problems,* **35** (10), 105004 (2019).

52. C. Jidling, N. Wahlstr\ m, A. Wills, and T. B. Sch\ n, 1215--1224 (2017).

53. A. Solin, M. Kok, N. Wahlström, T. B. Schön, and S. Särkkä, *IEEE Transactions on Robotics,* **34** (4), 1112-1127 (2018).

54. J. Hendriks, A. Gregg, C. Wensrich, and A. Wills, *Strain,* **55** (5), e12325 (2019).

55. F. Ciucci, *Gaussian-process Hilbert transform (GP-HT)*, https://github.com/ciuccislab/GP-HT.

56. M. Schönleber and E. Ivers-Tiffée, *Electrochem. Commun.,* **58** 15-19 (2015).

57. F. Ciucci and C. Chen, *Electrochim. Acta,* **167** 439-454 (2015).

58. M. B. Effat and F. Ciucci, *Electrochim. Acta,* **247** 1117-1129 (2017).

59. J. Liu and F. Ciucci, *J. Electrochem. Soc.,* **167** (2), 026506 (2020).

60. N. Murer, J.-P. Diard, and B. Petrescu, *J. Electrochem. Sci. Eng.,* **10** (2), 127-140 (2020).

61. E. Quattrocchi, T. H. Wan, A. Curcio, S. Pepe, M. B. Effat, and F. Ciucci, *Electrochim. Acta,* **324** 134853 (2019).

62. J. Liu, J. Wang, A. Belotti, and F. Ciucci, *ACS Appl. Energy Mater.,* **2** (8), 5472-5480 (2019).

63. J. Yu, Y.-Q. Lyu, J. Liu, M. B. Effat, S. C. T. Kwok, J. Wu, and F. Ciucci, *J. Mater. Chem. A,* **7** (30), 17995-18002 (2019).

64. J. Wu, J. Liu, J. Cui, S. Yao, M. Ihsan-Ul-Haq, N. Mubarak, E. Quattrocchi, F. Ciucci, and J.-K. Kim, *J. Mater. Chem. A,* (2020).

65. R. Ruffo, S. S. Hong, C. K. Chan, R. A. Huggins, and Y. Cui, *J. Phys. Chem. C,* **113** (26), 11390-11398 (2009).

66. J. Song and M. Z. Bazant, *Phys. Rev. Lett.,* **120** (11), 116001 (2018).

67. M. Durbha, M. E. Orazem, and L. H. Garcia‑Rubio, *J. Electrochem. Soc.,* **144** (1), 48 (1997).

Table 1 – Matrices, vectors, and scalars used for the GP-HT.

$X(\boldsymbol{\omega})$	$X_{\mathrm{H}}(\omega_\star)$	$\boldsymbol{K}$	$H\boldsymbol{k}_\star$	$H^2 k_{\star\star}$	β	$\boldsymbol{b}$
Hilbert Transform						
$\boldsymbol{Z}_{\mathrm{exp,im}}(\boldsymbol{\omega})$	$Z_{\mathrm{H,re}}(\omega_\star)$	$k_{\mathrm{im}}(\boldsymbol{\omega},\boldsymbol{\omega})$	$k_{\mathrm{im-re}}(\boldsymbol{\omega},\omega_\star)$	$k_{\mathrm{re}}(\omega_\star,\omega_\star)$	L_0	$\boldsymbol{\omega}$
$\boldsymbol{Y}_{\mathrm{exp,im}}(\boldsymbol{\omega})$	$Y_{\mathrm{H,re}}(\omega_\star)$	$k_{\mathrm{im}}(\boldsymbol{\omega},\boldsymbol{\omega})$	$k_{\mathrm{im-re}}(\boldsymbol{\omega},\omega_\star)$	$k_{\mathrm{re}}(\omega_\star,\omega_\star)$	C_0	$\boldsymbol{\omega}$
Regression						
$\boldsymbol{Z}_{\mathrm{exp,im}}(\boldsymbol{\omega})$	$Z_{\mathrm{im}}(\omega_\star)$	$k_{\mathrm{im}}(\boldsymbol{\omega},\boldsymbol{\omega})$	$k_{\mathrm{im}}(\boldsymbol{\omega},\omega_\star)$	$k_{\mathrm{im}}(\omega_\star,\omega_\star)$	L_0	$\boldsymbol{\omega}$
$\boldsymbol{Y}_{\mathrm{exp,im}}(\boldsymbol{\omega})$	$Y_{\mathrm{im}}(\omega_\star)$	$k_{\mathrm{im}}(\boldsymbol{\omega},\boldsymbol{\omega})$	$k_{\mathrm{im}}(\boldsymbol{\omega},\omega_\star)$	$k_{\mathrm{im}}(\omega_\star,\omega_\star)$	C_0	$\boldsymbol{\omega}$
	datatype	matrix $\mathbb{R}^{N\times N}$	vector $\mathbb{R}^{N\times 1}$	scalar $\mathbb{R}$	RV $\sim\mathcal{N}(0,\sigma_\beta^2)$	vector $\mathbb{R}^N$
Formulas						
$X_{\mathrm{H}}(\omega_\star)\mid\boldsymbol{X}(\boldsymbol{\omega})\sim\mathcal{N}\left(\mu_{X_H},\sigma_{X_H}^2\right)$	$\mu_{X_H} = H\boldsymbol{k}_\star^\top\left(\boldsymbol{K}+\sigma_n^2\boldsymbol{I}+\sigma_\beta^2\boldsymbol{b}\boldsymbol{b}^\top\right)^{-1}\boldsymbol{X}(\boldsymbol{\omega})$					
	$\sigma_{Z_H}^2 = H^2 k_{\star\star} - H\boldsymbol{k}_\star^\top\left(\boldsymbol{K}+\sigma_n^2\boldsymbol{I}+\sigma_\beta^2\boldsymbol{b}\boldsymbol{b}^\top\right)^{-1}H\boldsymbol{k}_\star$					

Figure 1 – Schematic illustration of the GP-HT method.
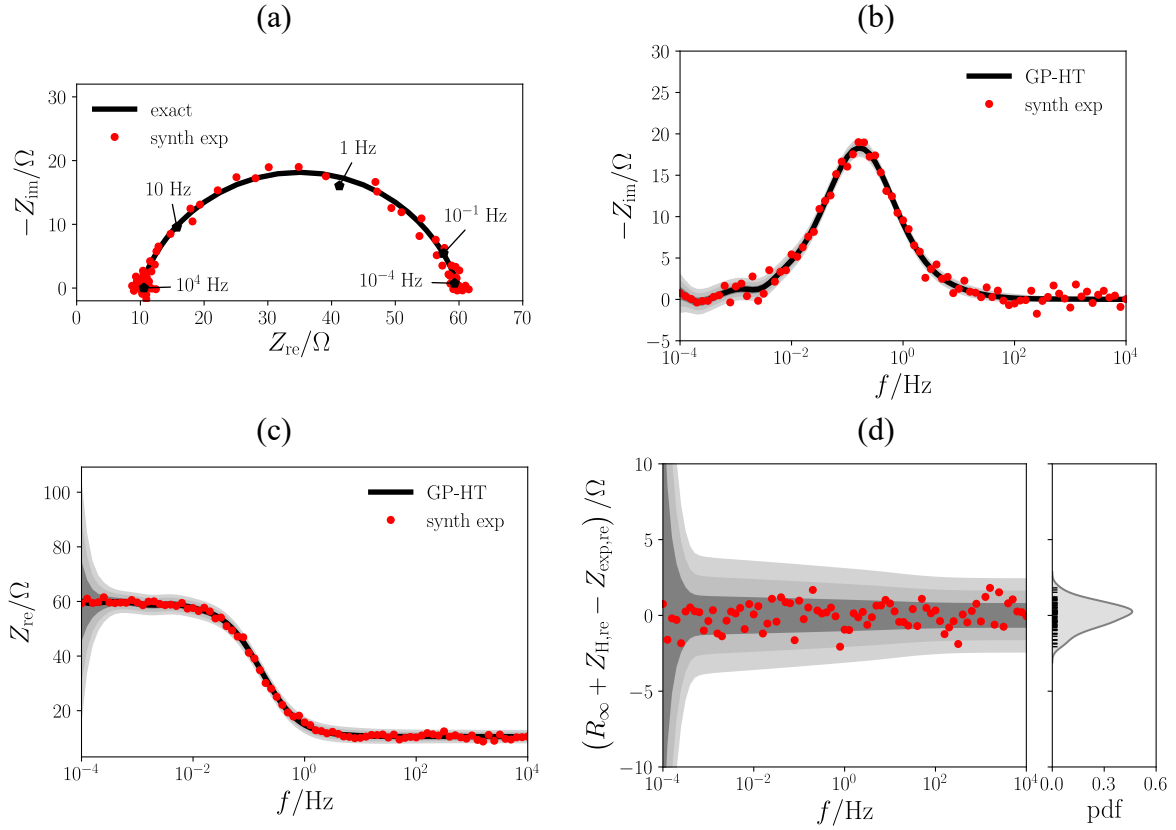
Figure 2 – (a) Nyquist plot of the synthetic impedance of a ZARC element, (b) imaginary part of the artificial impedance and its GP-HT regression, (c) real part of the synthetic experiment shown with the prediction from the GP-HT, and (d) residual plots. Solid black lines correspond to the predicted mean value, and the gray regions correspond to the 1σ, 2σ, and 3σ credible bands.
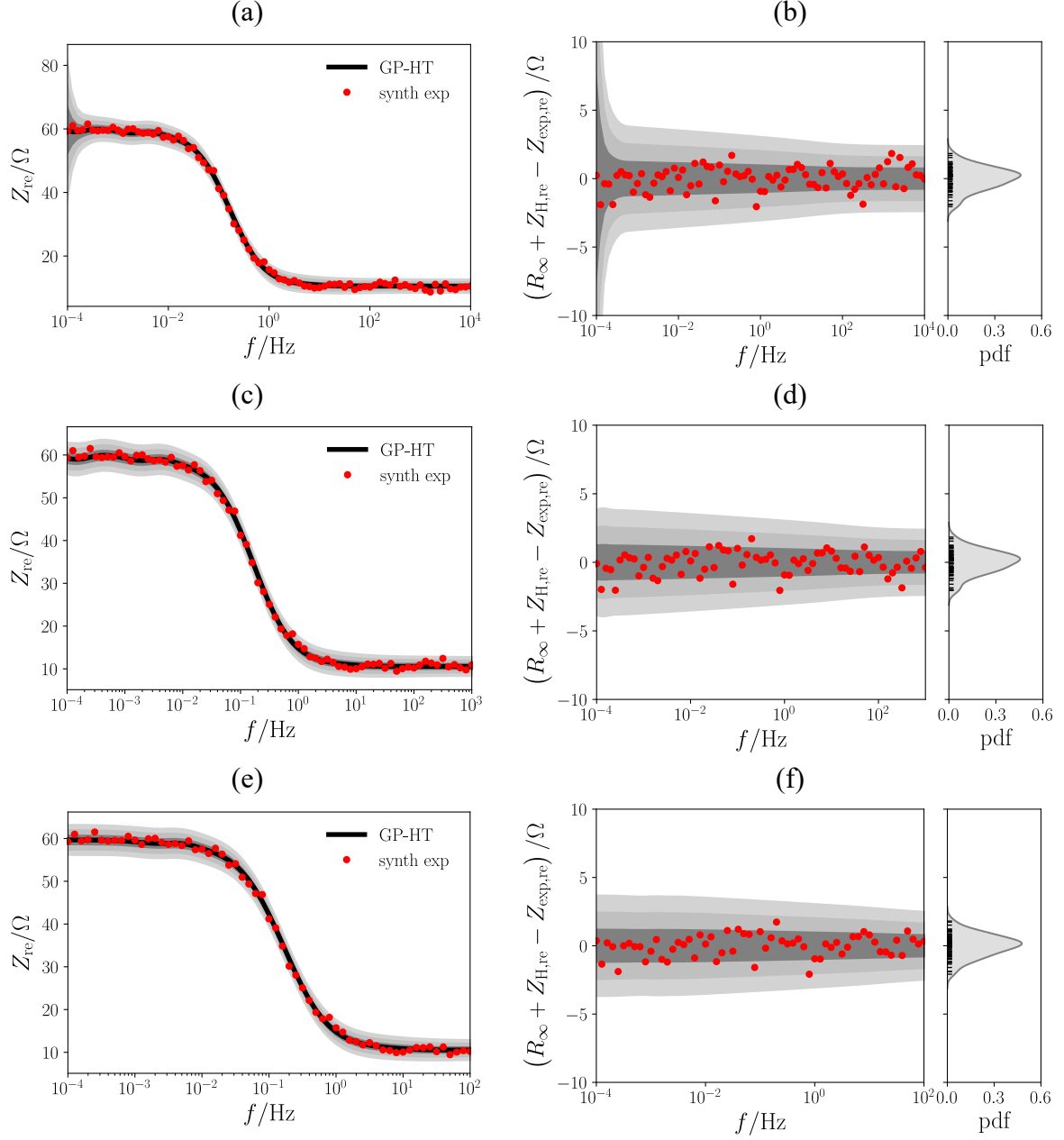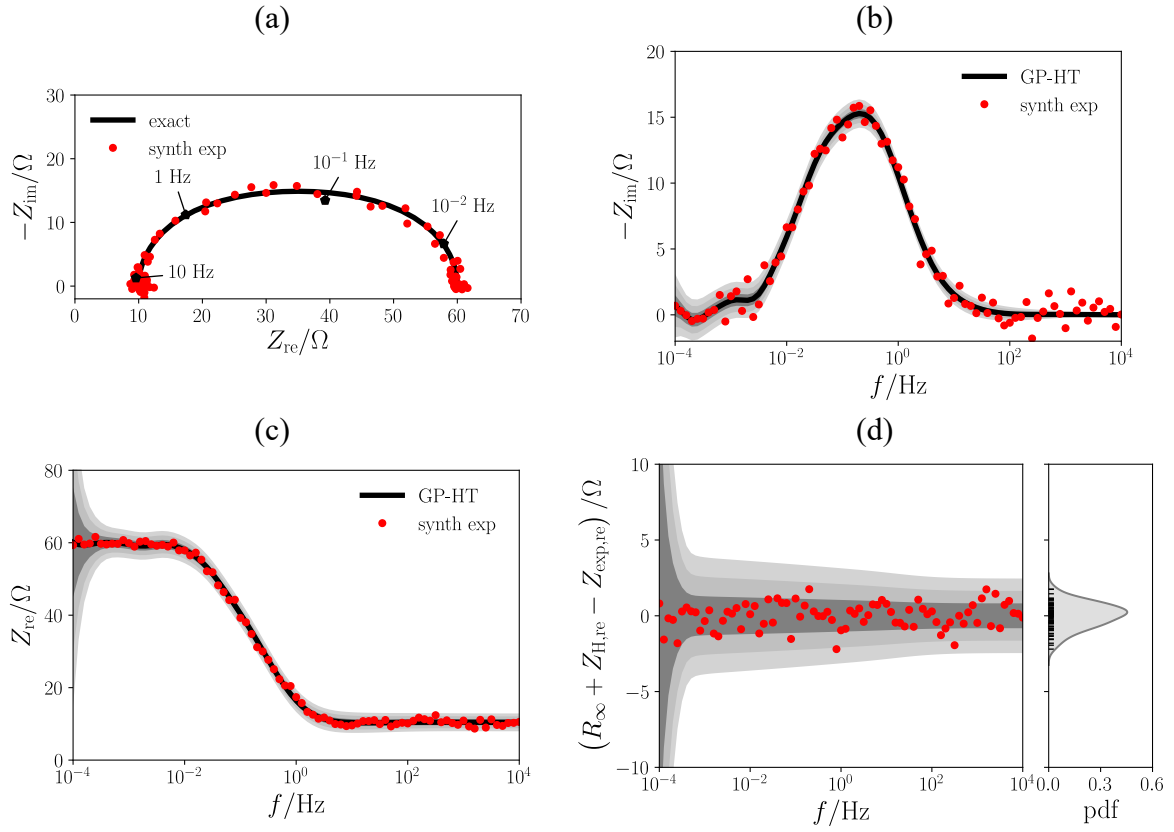
Figure 3 – Prediction via the GP-HT using the BL-DRT kernel from 0 to $\tau_{\max}$. (a), (c), and (e) real part of the synthetic experiment compared against prediction from the GP-HT, and (b), (d), and (f) residual plots. (a) and (b), $\tau_{\max} = 10^4$ s; (c) and (d), $\tau_{\max} = 10^3$ s; (e) and (f), $\tau_{\max} = 10^2$ s. Solid black lines correspond to the predicted mean value, and the grey-colored regions correspond to the 1σ, 2σ, and 3σ credible bands.

Figure 4 – (a) Nyquist plot of the synthetic impedance of a PWC element, (b) imaginary part of the impedance and corresponding GP-HT regression, (c) real part of the synthetic experiment shown together with the prediction from the GP-HT, and (d) residual plots.
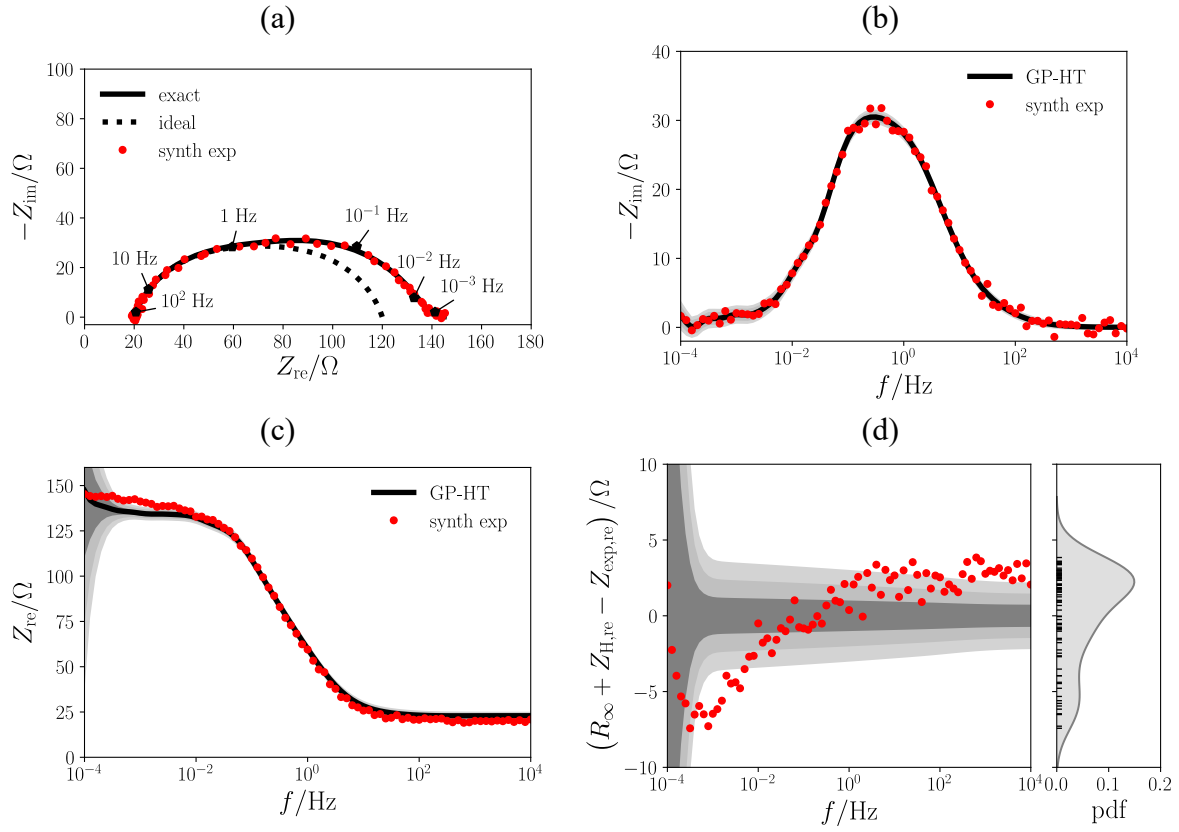
Figure 5 – Non-HT compliant impedance. (a) Nyquist plot of the synthetic EIS spectrum of the 2×ZARC with low-frequency drift, (b) imaginary and (c) real parts with corresponding GP-HT regression and predictions, and (d) associated residual plots. Deviations are shown in both panels (c) and (d) as the synthetic experiment does not satisfy the HT.
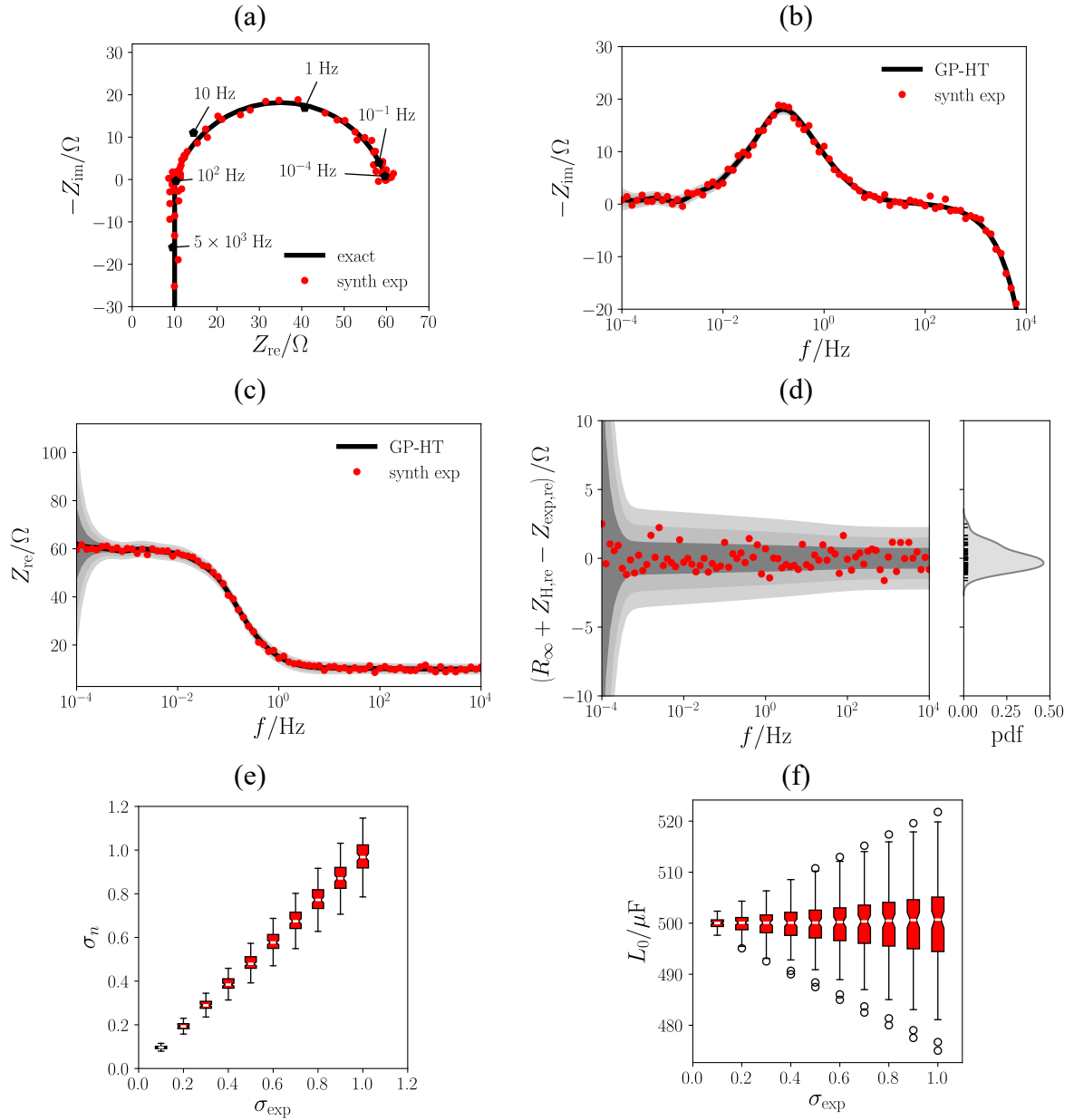
Figure 6 – (a) Nyquist plot of the synthetic impedance of a ZARC with the inductance, (b) imaginary part of the synthetic impedance and GP-HT regression, (c) real part of the simulated EIS spectrum and corresponding GP-HT prediction, and (d) residual plots. Boxplot of the (e) optimal hyperparameter σ_n and (e) estimated L_0 as a function of the imposed noise level σ_{exp}. In the boxplot the notch, box, and whiskers indicate the median, the 25 to 75% interquartile range (IQR), and 1.5 times the IQR, respectively; the circles represent the outliers.
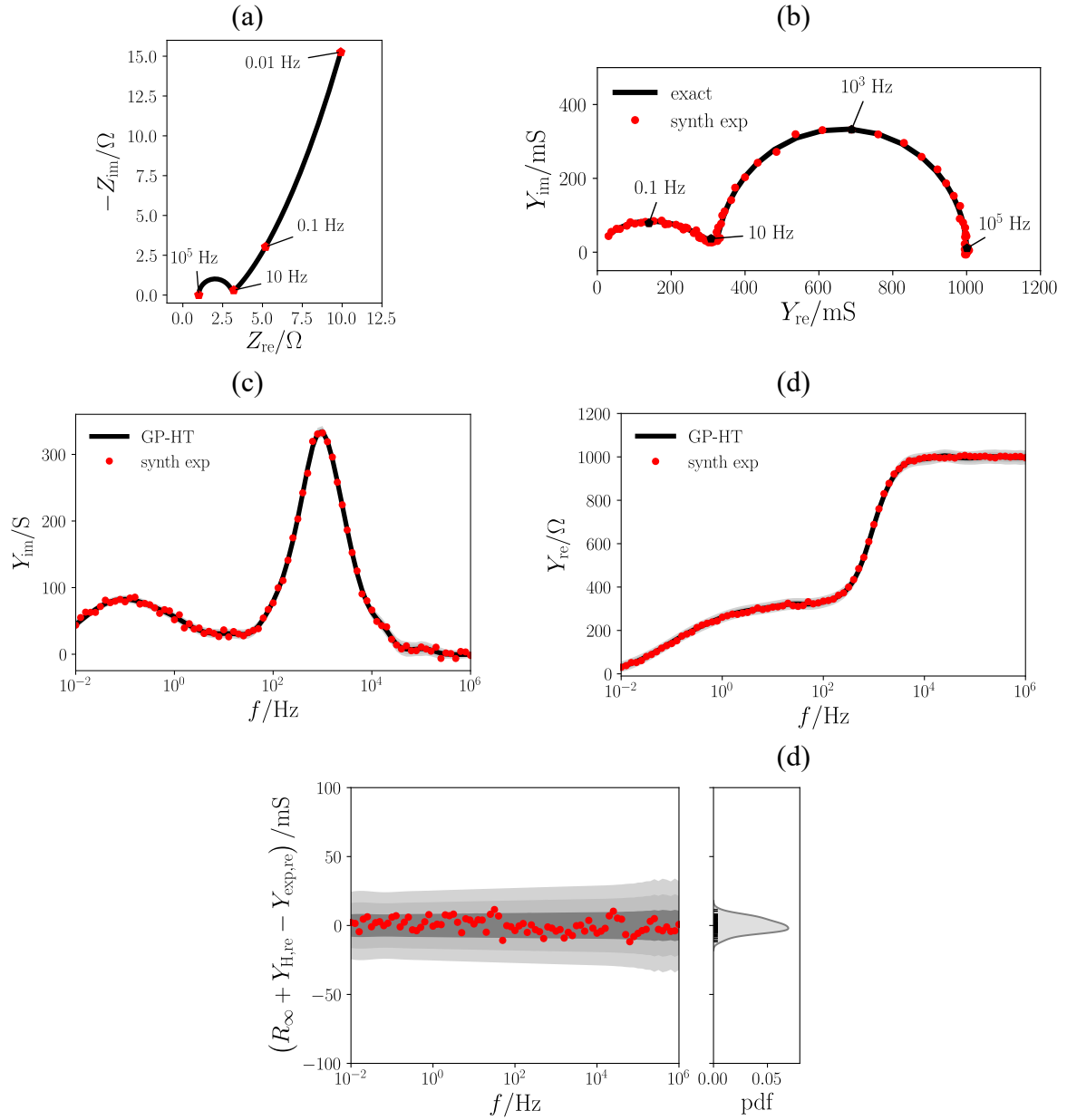
Figure 7 – Nyquist plot of (a) the exact impedance from the nonlinear DDT model, (b) the admittance of a realization of a synthetic experiment. (c) imaginary part of the admittance and its GP-HT regression, (d) GP-HT prediction compared against the real part of the artificial admittance, and (e) corresponding residual plots.
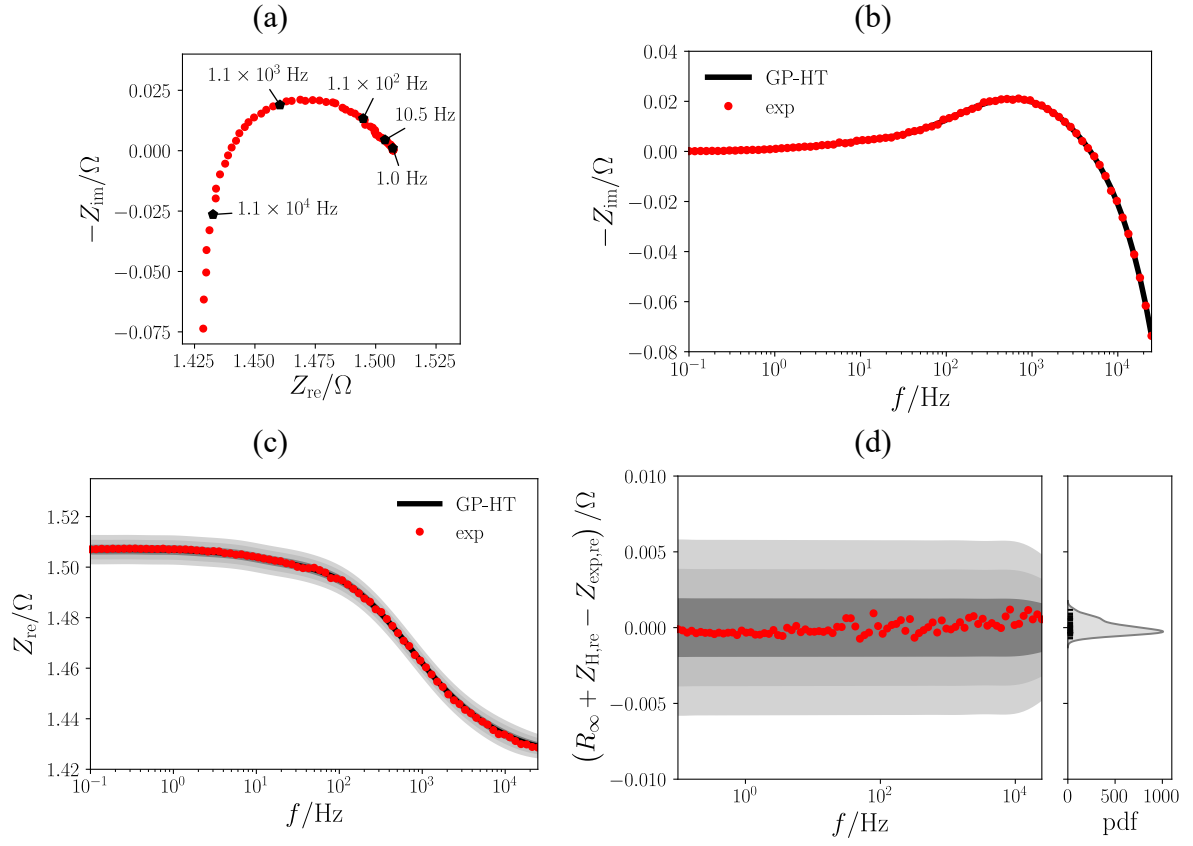
Figure 8 – (a) Nyquist plot of the impedance of BLFP, (b) imaginary part and GP-HT regression, (c) real component shown with the GP-HT prediction, and (d) residual plots.
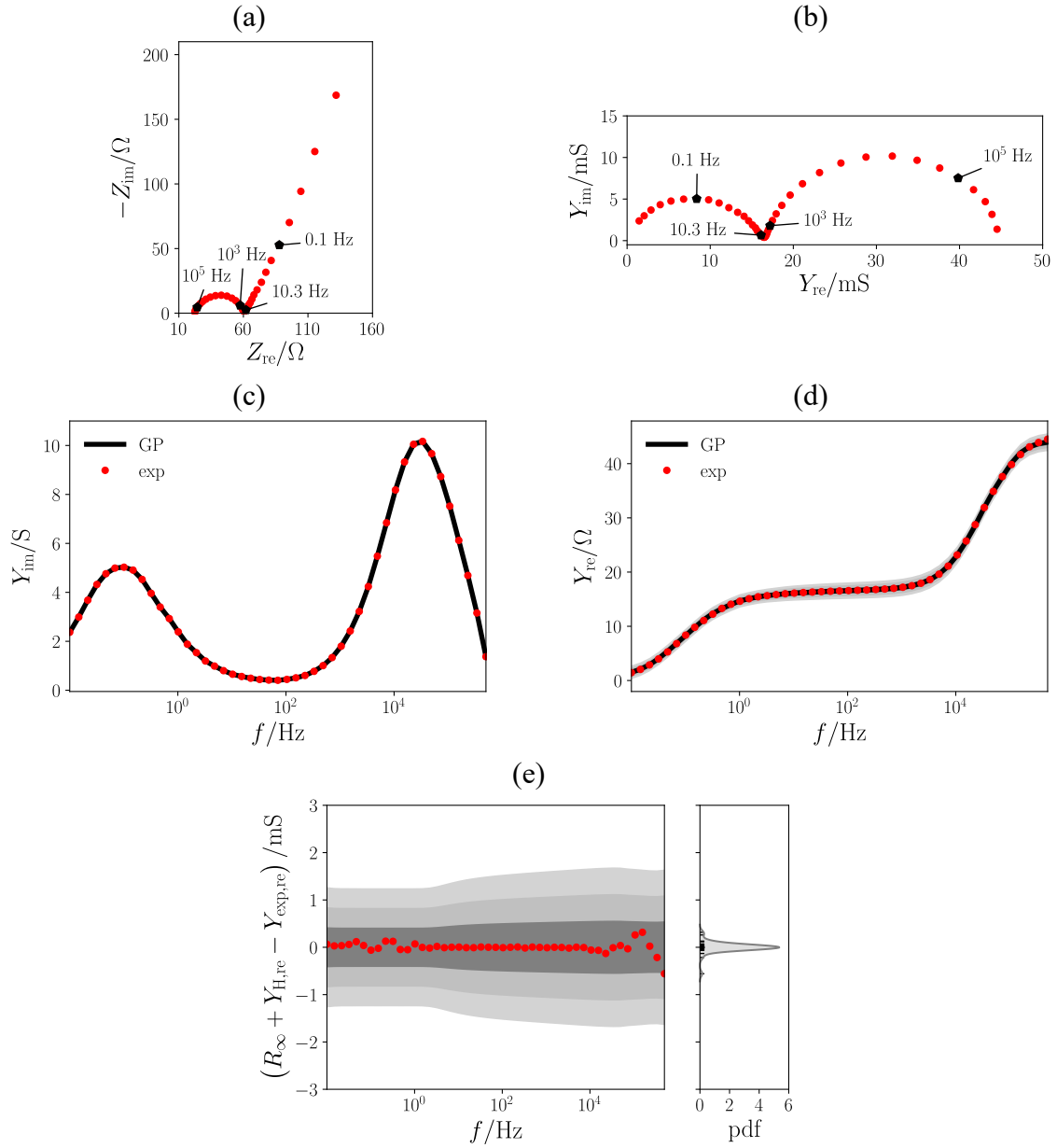
Figure 9 – Nyquist plot of the (a) impedance from the 2H-MoS$_2$ half-cell and (b) admittance. (c) the admittance's imaginary component and its GP-HT regression, and (d) GP-HT prediction versus the real part of the admittance. (e) residual plots comparing the GP-HT and the experimental data.

Supplementary Information

The Gaussian Process Hilbert Transform (GP-HT): Testing the

Consistency of Electrochemical Impedance Spectroscopy Data

Francesco Ciucci[a,b,†]

[a] Department of Mechanical and Aerospace Engineering, The Hong Kong University of Science and Technology, Hong Kong, China

[b] Department of Chemical and Biological Engineering, The Hong Kong University of Science and Technology, Hong Kong, China

[†]Corresponding author: francesco.ciucci@ust.hk
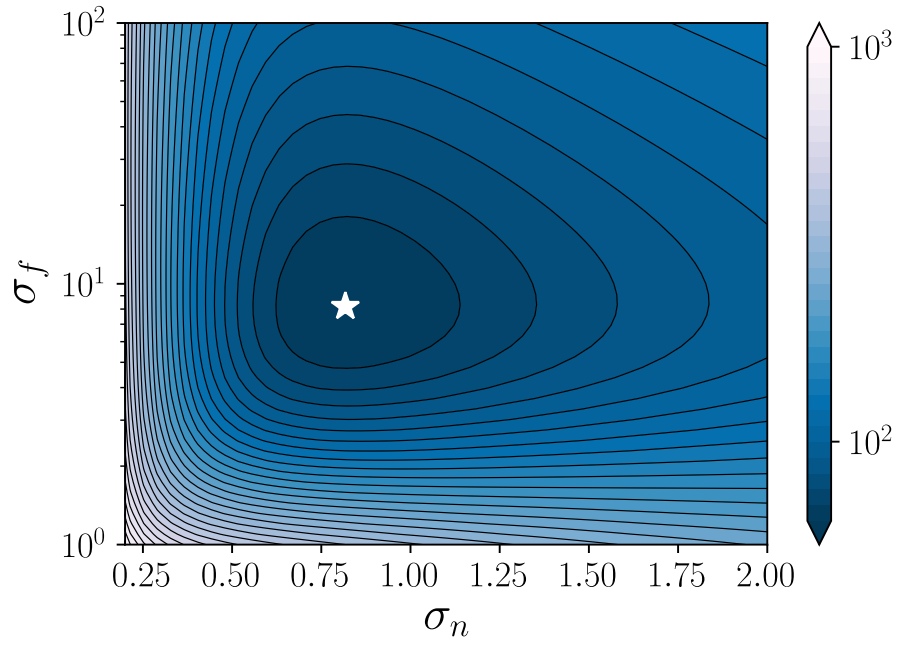
Figure S1 – Negative log-likelihood of the stochastic experiment shown in Figure 1 (a) as a function of the hyperparameters σ_n and σ_f. The location of the minimum is indicated with a star symbol.
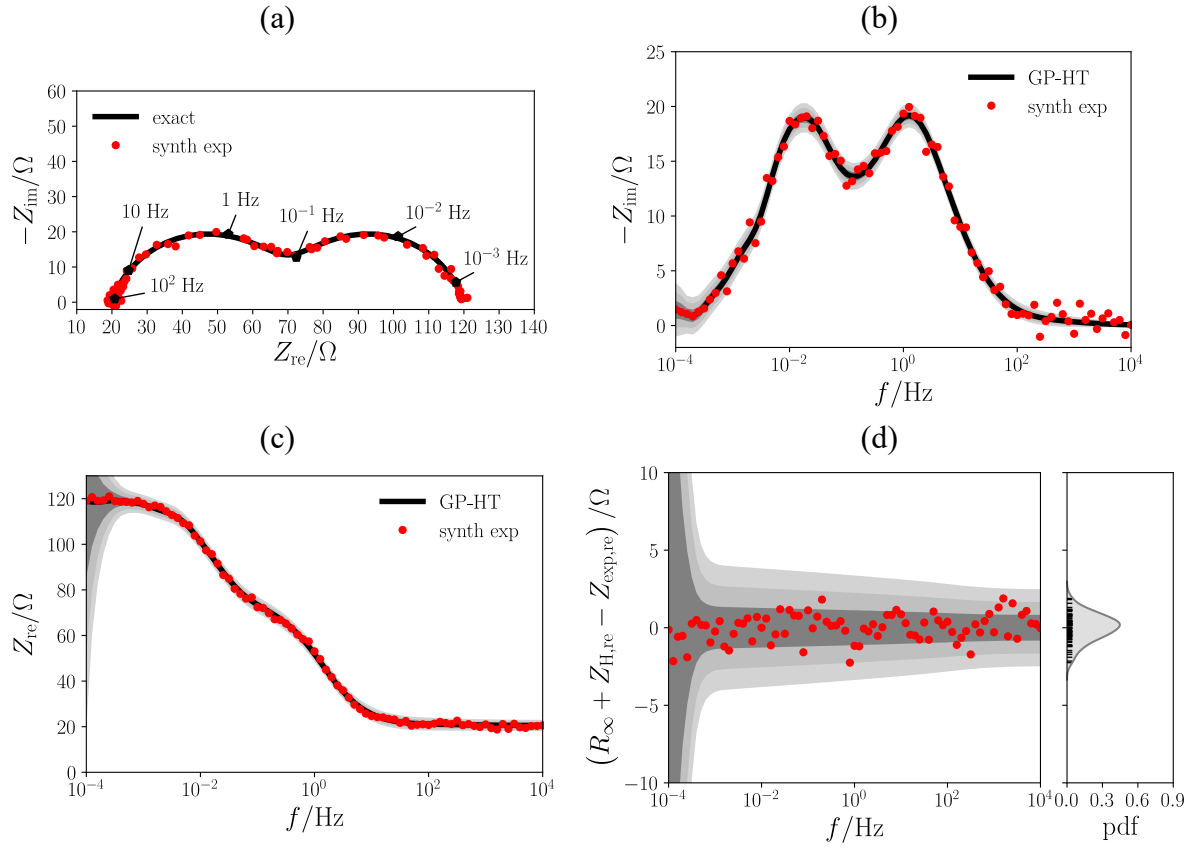
Figure S2 – (a) Nyquist plot of the synthetic impedance of a 2×ZARC element ($\tau_0^{\mathrm{I}} = 10^{-1}$ s and $\tau_0^{\mathrm{II}} = 10$ s), (b) imaginary part of the impedance and corresponding GP-HT regression, (c) real part of the synthetic experiment shown together with the prediction from the GP-HT, and (d) residual plots.
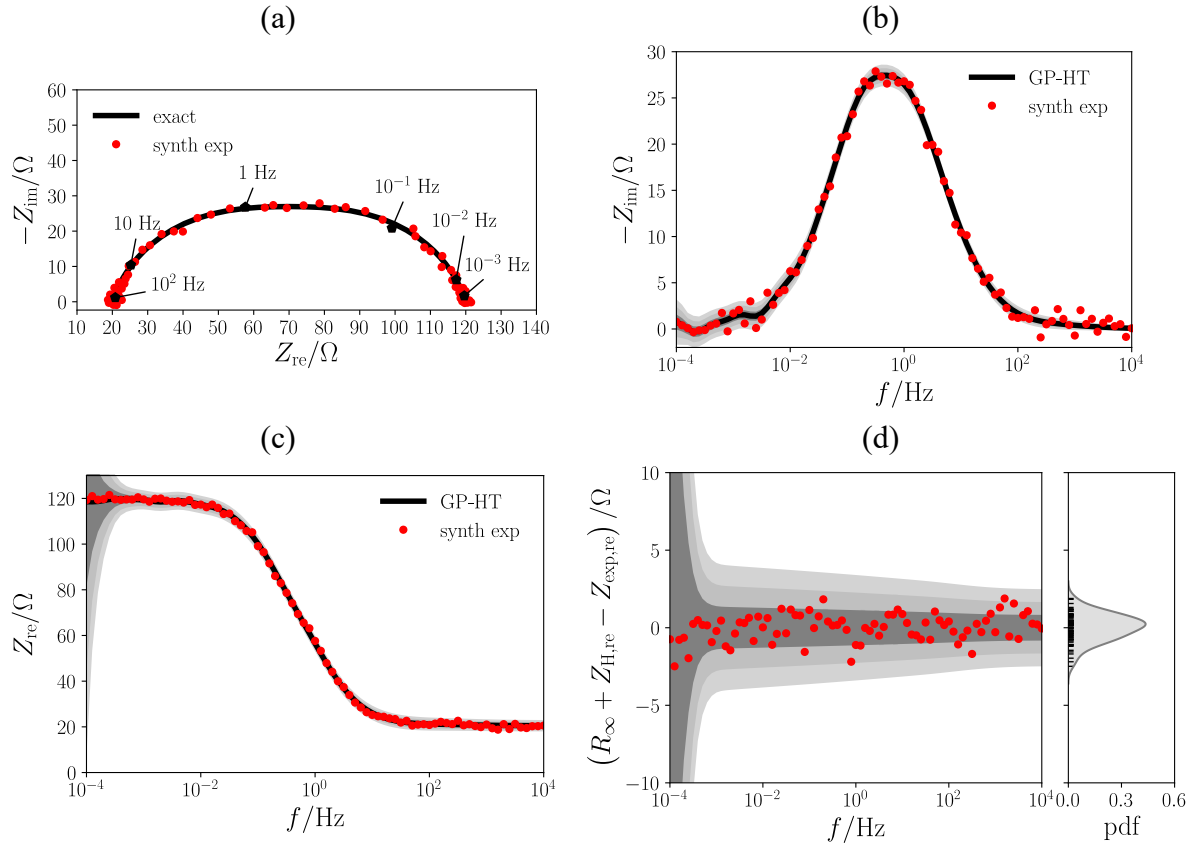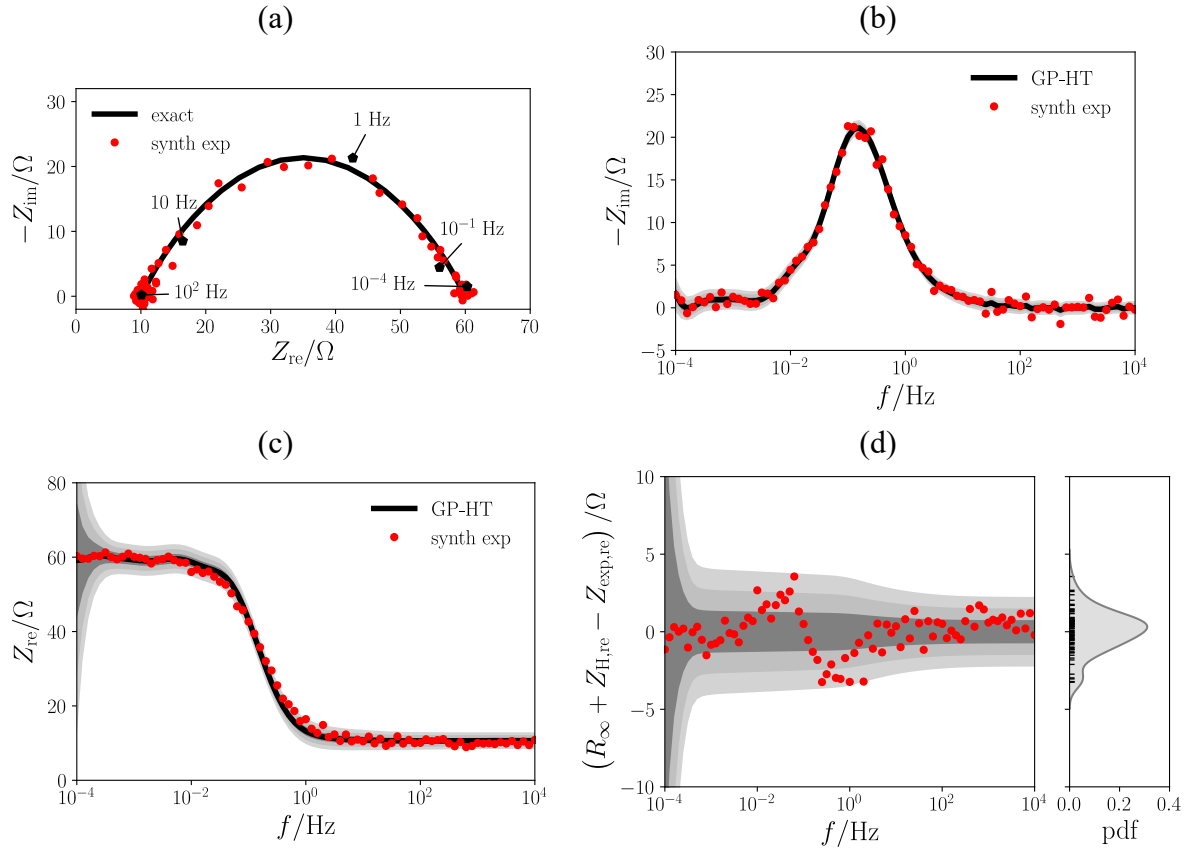
Figure S3 – (a) Nyquist plot of the synthetic impedance of a 2×ZARC element ($\tau_0^{\mathrm{I}} = 10^{-1}$ s and $\tau_0^{\mathrm{II}} = 1$ s), (b) imaginary part of the impedance and corresponding GP-HT regression, (c) real part of the synthetic experiment shown together with the prediction from the GP-HT, and (d) residual plots.
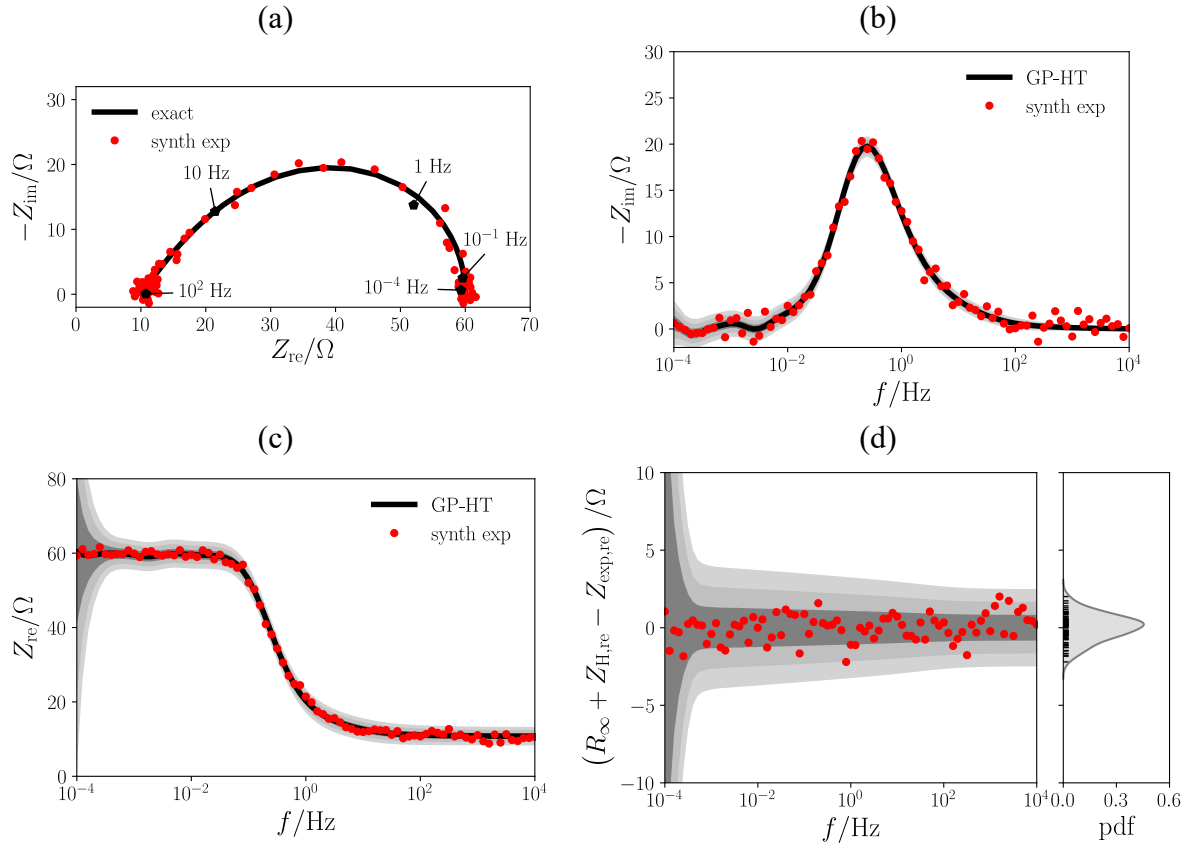
Figure S4 – (a) Nyquist plot of the synthetic impedance of a fractal element, (b) imaginary part of the impedance compared against the GP-HT regression, (c) real part of the synthetic experiment shown together with the GP-HT prediction, and (d) residual plots.

Figure S5 – Non-HT compliant impedance. (a) Nyquist plot of the synthetic EIS spectrum, (b) imaginary and (c) real parts with corresponding GP and GP-HT predictions. (d) residual plot.
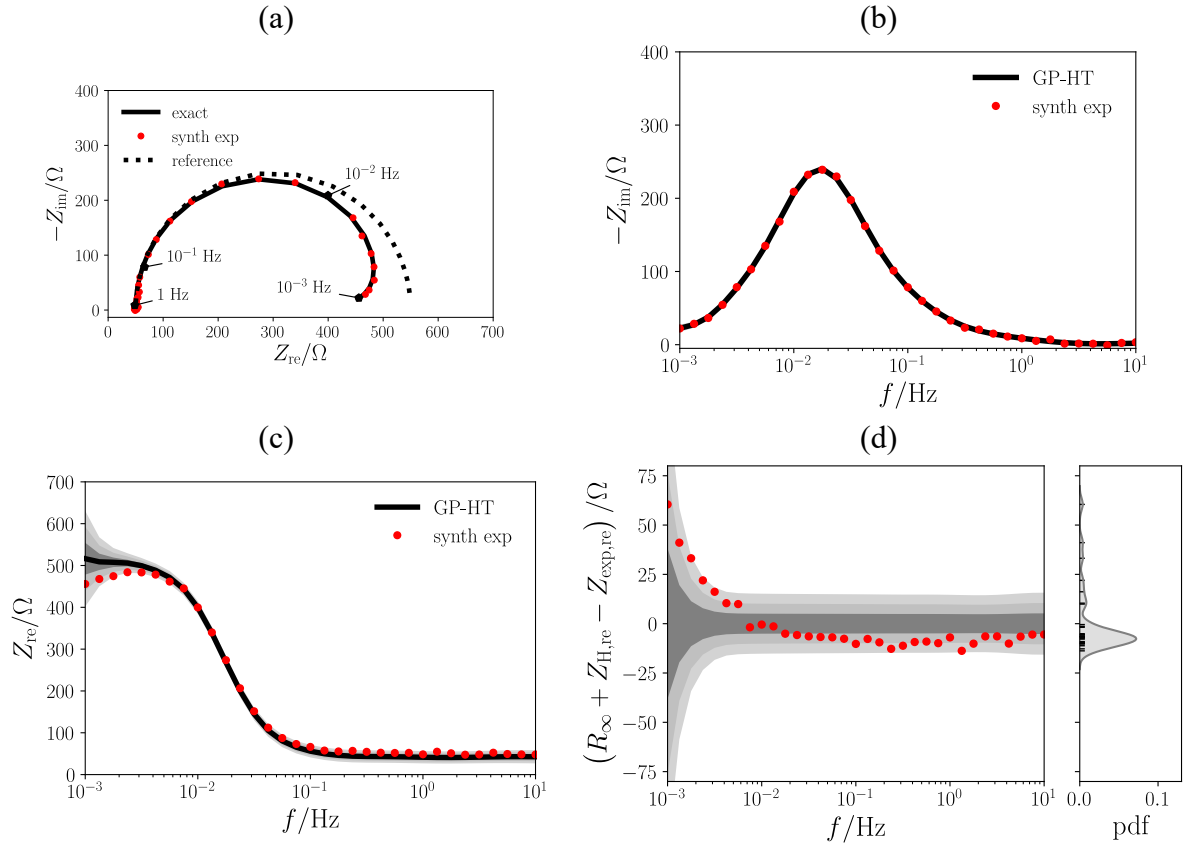
Figure S6 – Time-drifting impedance with a polarization resistance that decreases during the experiment. (a) Nyquist plot of the artificial EIS spectrum, (b) imaginary and (c) real parts with corresponding GP and GP-HT predictions. (d) residual plot.
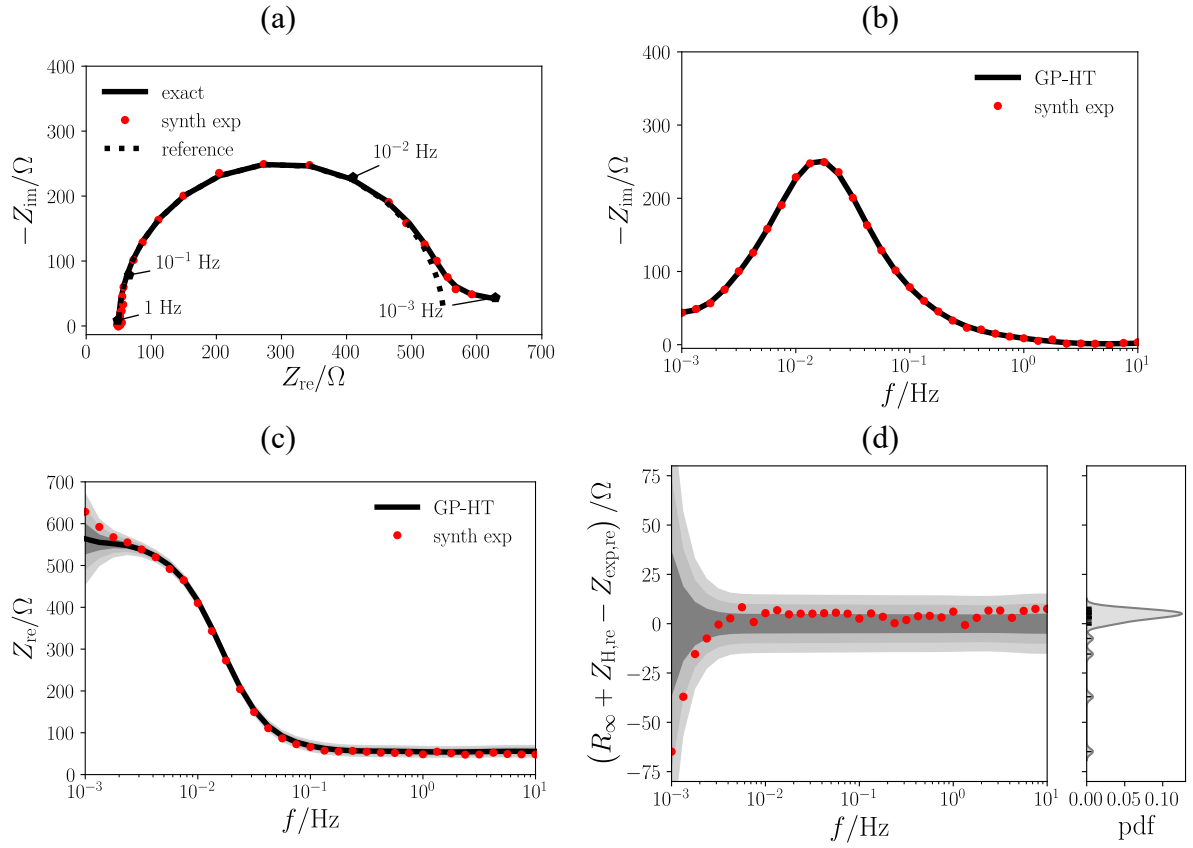
Figure S7 – Time-drifting impedance whose the polarization decreases during the experiment. (a) Nyquist plot of the artificial EIS spectrum, (b) imaginary and (c) real parts with corresponding GP and GP-HT predictions. (d) residual plot.
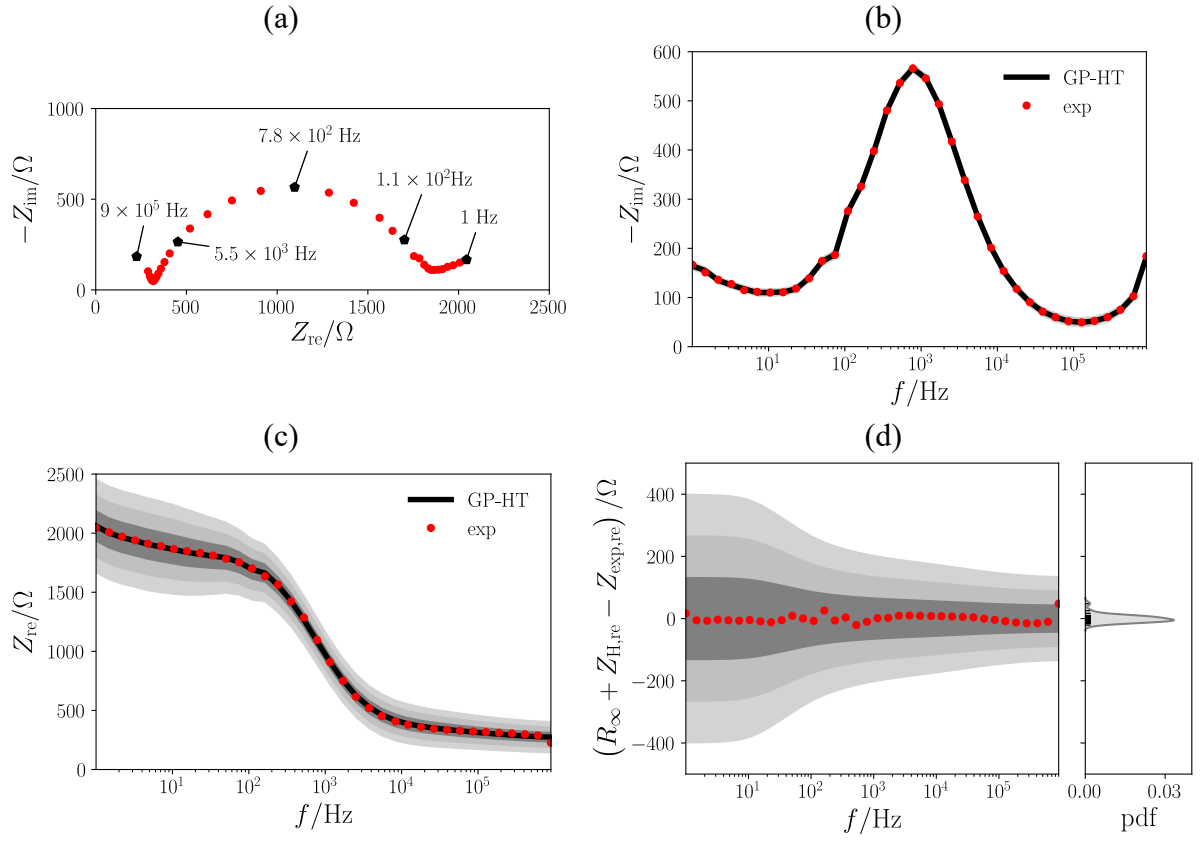
Figure S8 – (a) Nyquist plot of the impedance of a symmetrical Li-ion battery, (b) imaginary part and GP-HT regression, (c) real component of the EIS spectrum overlayed to the GP-HT prediction, and (d) residual plot.
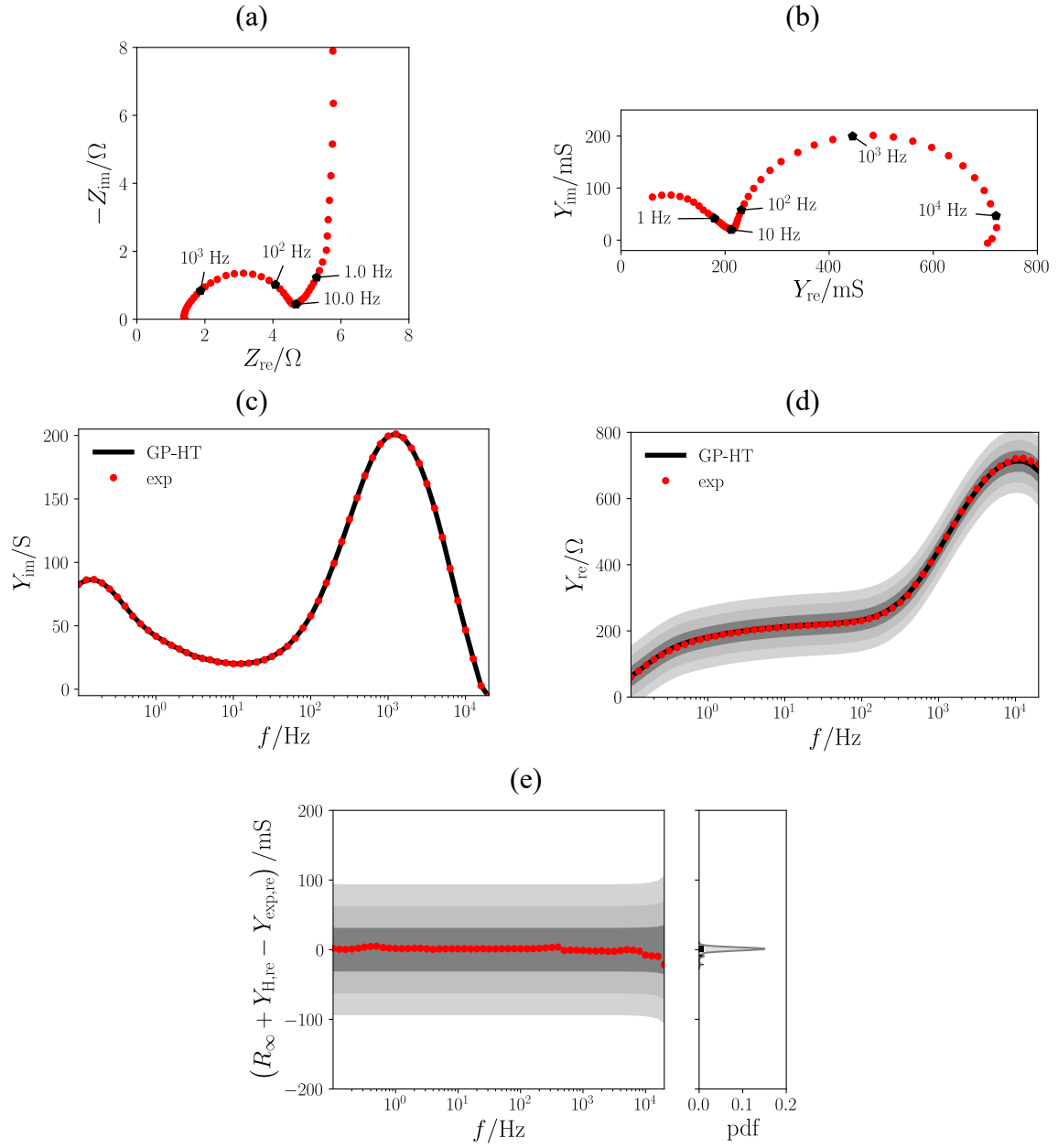
Figure S9 – Nyquist plot of the (a) impedance from the 2H-MoS2 half cell and (b) admittance. (c) the admittance's imaginary component and its GP-HT regression, and (d) GP-HT prediction versus the real part of the admittance, and (e) residual plots comparing the GP-HT and the experimental data.